Multi-Functional Reconfigurable Intelligent Surface: System Modeling and Performance Optimization

Wen Wang, Wanli Ni, Hui Tian, *Senior Member, IEEE,*
Yonina C. Eldar, *Fellow, IEEE,* and Rui Zhang, *Fellow, IEEE*

Abstract

In this paper, we propose and study a new multi-functional reconfigurable intelligent surface (MF-RIS) architecture. Different from conventional single-functional RIS (SF-RIS) that only reflects signals, the proposed MF-RIS can simultaneously support multiple functions with one surface, including reflection, refraction, amplification, and energy harvesting of wireless signals. As such, the proposed MF-RIS is capable of significantly enhancing the RIS signal coverage by amplifying the signal reflected/refracted by the RIS with the energy harvested. We present the signal model of the proposed MF-RIS, and formulate an optimization problem to maximize the sum-rate of multiple users in an MF-RIS-aided non-orthogonal multiple access network. By jointly optimizing the transmit beamforming, power allocations as well as the operating modes and parameters for different elements of the MF-RIS and its deployment location, we propose an iterative algorithm to solve this non-convex problem efficiently. Simulation results are provided which show significant performance gains of the MF-RIS over special cases with only some of its functions available. Moreover, we demonstrate that there exists a fundamental trade-off between sum-rate maximization and harvested energy maximization in MF-RIS. In contrast to SF-RISs which can be deployed near either the transmitter or receiver, the proposed MF-RIS should be deployed closer to the transmitter for maximizing its communication throughput with more energy harvested.

Index Terms

Multi-functional RIS, non-orthogonal multiple access, throughput maximization, energy harvesting, RIS deployment.

W. Wang, W. Ni, and H. Tian are with the State Key Laboratory of Networking and Switching Technology, Beijing University of Posts and Telecommunications, Beijing 100876, China (e-mail:{wen.wang, charleswall, tianhui}@bupt.edu.cn).

Y. C. Eldar is with the Math and CS Faculty, Weizmann Institute of Science, Rehovot 7610001, Israel (e-mail: yonina.eldar@weizmann.ac.il).

R. Zhang is with School of Science and Engineering, Shenzhen Research Institute of Big Data, The Chinese University of Hong Kong, Shenzhen, Guangdong 518172, China (e-mail: rzhang@cuhk.edu.cn). He is also with the Department of Electrical and Computer Engineering, National University of Singapore, Singapore 117583 (e-mail: elezhang@nus.edu.sg).

I. Introduction

Reconfigurable intelligent surfaces (RISs) or intelligent reflecting surfaces (IRSs) have emerged as a promising paradigm for future communication networks, due to their merits in improving the energy-efficiency and spectrum-efficiency in a low-cost manner [1], [2]. Through modifying the phase shift and/or amplitude of incident signals, RISs are able to establish a tunable communication environment for achieving various objectives, such as throughput maximization [3], [4], security enhancement [5], [6], energy reduction [7], and improved performance fairness [8]. However, due to hardware constraints, conventional single-functional RIS (SF-RIS) only supports signal reflection or refraction/transmission, and thus can only serve users located on one side of a RIS [3], [4]. The half-space coverage issue faced by SF-RIS greatly restricts the flexibility and effectiveness when deploying SF-RISs in wireless networks with randomly distributed users.

To overcome this limitation, the authors of [9]–[11] proposed new RIS architectures, termed simultaneously transmitting and reflecting reconfigurable intelligent surface (STAR-RIS) and intelligent omni-surface (IOS), by supporting signal reflection and refraction with one surface at the same time. Compared to the SF-RIS [3]–[8], such dual-functional RIS (DF-RIS) [9]–[11] is able to create a ubiquitous smart radio environment by providing full-space signal coverage. Moreover, the works [12] and [13] studied the benefits of DF-RIS-aided multi-user wireless communication networks in terms of coverage extension and security enhancement, respectively. However, due to the fact that the signal reflected/refracted by the RIS is attenuated twice, the signal path loss can be practically severe for both SF- and DF-RISs.

With the aim of combating the double attenuation faced by existing passive RISs, recent works such as [14] and [15] have proposed an active RIS architecture by embedding power amplifiers into conventional SF-RISs. The theoretical and simulation results in [16] and [17] showed that by properly designing the phase shift and amplification factors, active RISs yield significant spectrum efficiency gains compared to passive RISs. In addition, the authors of [18] proposed another metasurface architecture enabling signal amplification, known as dynamic metasurface antennas (DMAs). As an efficient way to realize active massive antenna arrays, DMAs enable different levels of amplification and phase shift on incident signals, thus overcoming the severe path loss issue with passive RISs. However, both active RISs and DMAs require additional energy consumption to maintain the operation of active components, which makes their performance highly dependent on the availability of the external power supply. In practice, the aforementioned

TABLE I
COMPARISON OF THE PROPOSED MF-RIS WITH SF- AND DF-RIS

RIS type	SF-RIS		DF-RIS			MF-RIS
	Reflecting-only RIS [1],[2], [4]-[8]	Transmitting-only RIS [3]	STAR-RIS/IOS [9]-[13]	Active RIS [14]-[17]	Self-sustainable RIS [19]-[21]	**This work**
Signal propagation illustration	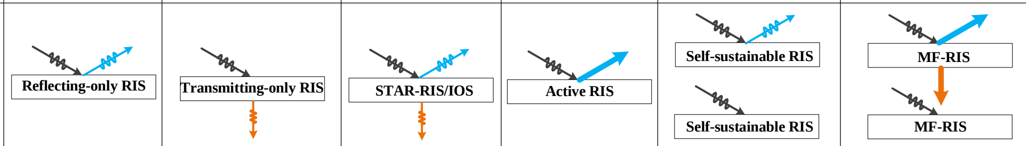					
Function support	Signal reflection	Signal refraction	Signal reflection and refraction	Signal reflection and amplification	Signal reflection and energy harvesting	Signal reflection, refraction, amplification, and energy harvesting
Full-space coverage			√			√
Path loss mitigation				√		√
Self-sustainability					√	√

RIS architectures are powered by battery or grid [1], [2]. For battery-powered RISs, embedded batteries only provide limited lifetime and cannot support the long-term operation of RISs. Given the environmental hazard and hardware limitation, replacing the battery of RISs manually may be costly and impractical [19]. While for grid-powered RISs, their deployment locations are limited because not all places are reachable for power line networks [20], [21]. Therefore, it is important to develop new RIS architectures that are capable of achieving their self-sustainability while maintaining the performance advantages of state-of-the-art RISs.

In this paper, we propose a new multi-functional RIS (MF-RIS) architecture aiming to overcome the aforementioned drawbacks faced by existing RISs, such as half-space coverage, double attenuation, and reliance on battery/grid. In Table I, we compare the existing SF- and DF-RIS with the proposed MF-RIS in terms of signal propagation model and design metrics. It can be seen that the DF-RISs only partially address the challenges that limit the flexibility and effectiveness of SF-RISs. In contrast, the proposed MF-RIS utilizes the energy harvested from radio-frequency (RF) signals to support the simultaneous reflection, refraction/transmission, and amplification of incident signals. Therefore, the proposed MF-RIS is able to achieve full-space coverage and path loss mitigation in a self-sustainable manner, thereby providing efficient and uninterrupted communication services to users in the whole space. In particular, by allowing all the elements to flexibly switch between different operating modes, the proposed MF-RIS offers more degrees of freedom (DoFs) for signal manipulation. To validate the throughput performance improvement when applying MF-RIS in wireless networks, we investigate a sum-rate maximization problem in an MF-RIS-aided non-orthogonal multiple access (NOMA) network.

The main contributions of this paper are summarized as follows:

- First, we propose an MF-RIS architecture with multiple functions such as signal reflection, refraction, amplification, and energy harvesting. Specifically, we design the operating protocol for the proposed MF-RIS to work in wireless networks. By comparing the differences between the MF-RIS and existing RISs in terms of signal models, it is shown that the MF-RIS is a general architecture that incorporates existing RISs as special cases.
- Second, we formulate an optimization problem to maximize the sum-rate of multiple users in an MF-RIS-aided NOMA network by jointly optimizing the transmit beamforming, power allocations as well as the operating modes and parameters for different elements of the MF-RIS and its deployment location. This problem is a mixed-integer non-linear programming (MINLP) problem, which is non-convex and thus difficult to be optimally solved. To tackle this problem, we propose an alternating optimization (AO)-based algorithm to find a high-performance suboptimal solution for it efficiently.
- Finally, extensive simulation results are provided which show that: 1) compared to the conventional passive RIS and self-sustainable RIS, the proposed MF-RIS attains 23.4% and 98.8% performance gains, respectively; 2) due to the limited number of RIS elements, there exists a fundamental trade-off between sum-rate maximization and energy harvesting performance for the MF-RIS; 3) different from SF-RISs which can be deployed near either the transmitter or receiver, the proposed MF-RIS should be deployed closer to the transmitter for maximizing its communication throughput with more energy harvested.

The rest of this paper is organized as follows. Section II provides the operation design and signal model of MF-RIS. Section III presents the system model and problem formulation of an MF-RIS-aided NOMA network. The resulting MINLP problem is efficiently solved in Section IV. Numerical results are presented in Section V, followed by conclusions in Section VI.

II. Operation Design and Signal Model of MF-RIS

In this section, we first give a brief introduction of the operation mechanism of the proposed MF-RIS. Then, we present the signal model of MF-RIS-aided wireless communications.

A. Operation Design

As shown in Fig. 1, each element of the MF-RIS can operate in two modes: energy harvesting mode (H mode) and signal relay mode (S mode). By flexibly adjusting the circuit connection, each element can switch between the H mode and S mode. These elements operating in H mode

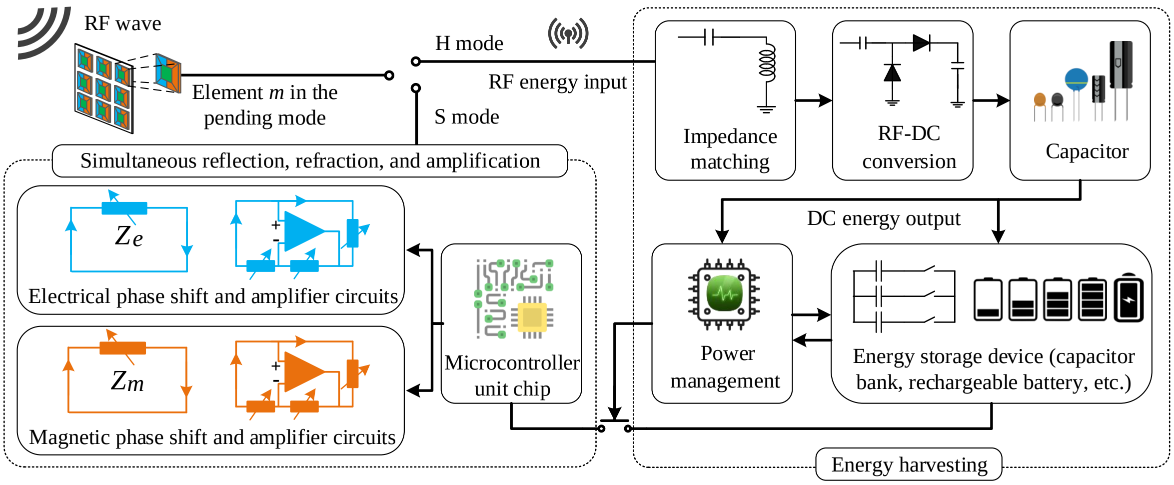

Fig. 1. A schematic diagram of the proposed MF-RIS.

can harvest RF energy from the incident signal, and convert it to direct current (DC) power for supporting the operation of the MF-RIS[1]. The energy harvesting circuit mainly consists of the following components [22], [23]:

- An impedance matching network consisting of a high quality factor resonator is invoked to guarantee the maximum power transmission from the element to the rectifier block.
- An RF-DC conversion circuit rectifies the available RF power into DC voltage.
- Capacitors are used to ensure that the current is delivered smoothly to the energy storage device, or as a short-term reserve when RF energy is unavailable.
- A power management block decides whether to store the converted electricity energy or use it immediately for signal reflection, refraction, and amplification.
- Energy storage devices (e.g., rechargeable batteries and super capacitors) are used to store energy. Whenever the harvested energy exceeds the consumption, any excess will be stored for future use, thus achieving continuous self-sustainability.

For other elements operating in S mode, the incident signals are divided into two parts by manipulating the electric and magnetic currents. One part is reflected to the reflection half-space and the other part is refracted to the other refraction half-space. With the aid of a microcontroller unit, these elements can leverage the harvested energy to sustain the operation of phase-shifting and amplifier circuits. Therefore, the proposed MF-RIS does not need any external

[1]Compared to solar energy, RF energy harvesting is capable of operating indoors or in low-light environments, as well as having higher power densities [22]. Furthermore, the mechanism of using solar energy as a renewable and eco-friendly power supply for RISs can also be incorporated in our MF-RIS system model and design.

power supply in principle. The schematic diagrams of the reflection and refraction amplifiers are also shown in Fig. 1, where the operational amplifier-based current-inverting converters are used to generate the reflected and refracted signals with desired amplification. Regarding the practical implementation of MF-RIS, there have been many research contributions on the prototype design of signal reflection [24], refraction [25], [26], amplification [15], and wireless power transfer [27]. These existing prototypes in [15], [24]–[27] have laid a strong practical foundation and provided valuable technical guidance for implementing the proposed MF-RIS[2].

B. Signal Model

In order to characterize the signal model of MF-RIS, we consider an MF-RIS having M elements, where the set of MF-RIS elements is indexed by $\mathcal{M} = \{1, 2, \cdots, M\}$. Let s_m denote the signal received by the m-th element. Due to the hardware limitation, we consider that each element cannot simultaneously work in both H and S modes. As such, the signals harvested, reflected, and refracted by the m-th element are modeled as $y_m^h = (1 - \alpha_m)s_m$, $y_m^r = \alpha_m\sqrt{\beta_m^r}e^{j\theta_m^r}s_m$, and $y_m^t = \alpha_m\sqrt{\beta_m^t}e^{j\theta_m^t}s_m$, respectively, where $\alpha_m \in \{0, 1\}$, $\theta_m^r, \theta_m^t \in [0, 2\pi)$, and $\beta_m^r, \beta_m^t \in [0, \beta_{\max}]$ denote the energy harvesting coefficient, the reflective and refractive phase shifts, and the reflective and refractive amplitude coefficients, respectively. Here, $\alpha_m = 1$ implies that the m-th element operates in S mode, while $\alpha_m = 0$ implies that it works in H mode, and $\beta_{\max} \geq 1$ denotes the amplification factor. Due to the law of energy conservation, the energy consumed by the amplifier should not exceed the maximum available energy that can be applied by the MF-RIS, i.e., $\beta_m^r + \beta_m^t \leq \beta_{\max}$. The reflective and refractive coefficients of MF-RIS are modeled as $\mathbf{\Theta}_r = \mathrm{diag}(\alpha_1\sqrt{\beta_1^r}e^{j\theta_1^r}, \alpha_2\sqrt{\beta_2^r}e^{j\theta_2^r}, \cdots, \alpha_M\sqrt{\beta_M^r}e^{j\theta_M^r})$ and $\mathbf{\Theta}_t = \mathrm{diag}(\alpha_1\sqrt{\beta_1^t}e^{j\theta_1^t}, \alpha_2\sqrt{\beta_2^t}e^{j\theta_2^t}, \cdots, \alpha_M\sqrt{\beta_M^t}e^{j\theta_M^t})$, respectively, where $\alpha_m \in \{0, 1\}$, $\beta_m^r, \beta_m^t \in [0, \beta_{\max}]$, $\beta_m^r + \beta_m^t \leq \beta_{\max}$, and $\theta_m^r, \theta_m^t \in [0, 2\pi)$.

The design variables and constraints for SF-, DF-, and MF-RIS are summarized in Table II. We observe that, mathematically, both SF- and DF-RISs can be regarded as special cases of the MF-RIS. For example, when $\alpha_m = 1$ and $\beta_{\max} = 1$, the MF-RIS reduces to the STAR-RIS in [9]; when α_m=1, $\beta_{\max} = 1$, $\beta_m^t = 0$, and $\theta_m^t = 0$, the MF-RIS reduces to the reflecting-only RIS in [1]. In addition, Table II shows that the proposed MF-RIS has more design variables than SF- and

[2]One noteworthy development is the use of tunnel diode-based amplifiers, which have significantly reduced the power consumption of amplifiers to the microwatt level, enabling the MF-RIS to achieve signal amplification in a lightweight and energy-efficient manner [28]. Furthermore, recent progress in thin-film capacitors, multi-level converters, and integrated power management has resulted in a considerable reduction in the implementation costs of energy harvesting circuits and an improvement in their harvesting efficiency [29]–[31].

TABLE II
COMPARISON OF SF-, DF-, AND MF-RIS IN TERMS OF DESIGN VARIABLES

RIS architecture		Design variable		
		Energy harvesting	Amplitude coefficient	Phase shift
SF-RIS	Reflecting-only RIS [1]	$\alpha_m = 1$	$\beta_m^r \in [0,1]$	$\theta_m^r \in [0, 2\pi)$
	Transmitting-only RIS [3]	$\alpha_m = 1$	$\beta_m^t \in [0,1]$	$\theta_m^t \in [0, 2\pi)$
DF-RIS	STAR-RIS/IOS [9]	$\alpha_m = 1$	$\beta_m^r, \beta_m^t \in [0,1]$	$\theta_m^r, \theta_m^t \in [0, 2\pi)$
	Active RIS [14]	$\alpha_m = 1$	$\beta_m^r \in [0, \beta_{\max}]$	$\theta_m^r \in [0, 2\pi)$
	Self-sustainable RIS [19]	$\alpha_m \in \{0,1\}$	$\beta_m^r \in [0,1]$	$\theta_m^r \in [0, 2\pi)$
MF-RIS (This work)		$\alpha_m \in \{0,1\}$	$\beta_m^r, \beta_m^t \in [0, \beta_{\max}]$, $\beta_m^r + \beta_m^t \leq \beta_{\max}$	$\theta_m^r, \theta_m^t \in [0, 2\pi)$

Note: By changing the load resistance/impedance of RIS elements, a certain portion of the energy of incident signals can be converted into heat and dissipated [1]. Therefore, passive RIS types achieve controllable amplitudes within the range of $[0, 1]$. In contrast, active RIS types extend the amplitude coefficient range to $[0, \beta_{\max}]$ with $\beta_{\max} \geq 1$ by utilizing active loads.

DF-RIS. This implies that while the MF-RIS offers more DoFs for signal manipulation, it also requires higher optimization complexity and incurs more overhead in exchanging configuration information between the base station (BS) and the MF-RIS. In Sections V and VI, we discuss some methods for simplifying the MF-RIS design to facilitate its practical use.

III. SYSTEM MODEL AND PROBLEM FORMULATION

A. Network Model

We consider an MF-RIS assisted downlink NOMA network[3], where an N-antenna BS serves J single-antenna users with the aid of an MF-RIS consisting of M elements. We denote the reflection (refraction) spatial direction as r (t). The spatial direction set and the user set are denoted by $\mathcal{K} = \{r, t\}$ and $\mathcal{J} = \{1, 2, \cdots, J\}$, respectively. We denote $\mathcal{J}_k = \{1, 2, \cdots, J_k\}$ as the set of users located in direction k and $\mathcal{J}_r \cup \mathcal{J}_t = \mathcal{J}$. For notation simplicity, we index user j in direction k by U_{kj}. Furthermore, we consider a three-dimensional (3D) Cartesian coordinate system with the locations of the BS, MF-RIS, and user U_{kj} being $\mathbf{w}_b = [x_b, y_b, z_b]^{\mathrm{T}}$, $\mathbf{w} = [x, y, z]^{\mathrm{T}}$, and $\mathbf{w}_{kj} = [x_{kj}, y_{kj}, 0]^{\mathrm{T}}$, respectively. In practice, due to the limited coverage of MF-RIS, its deployable region is also limited. Denote $\mathcal{P}$ as the predefined region for MF-RIS deployment, then the following constraint should be satisfied:

$$\mathbf{w} \in \mathcal{P} = \left\{ [x, y, z]^{\mathrm{T}} \left| x_{\min} \leq x \leq x_{\max}, y_{\min} \leq y \leq y_{\max}, z_{\min} \leq z \leq z_{\max} \right. \right\}, \tag{1}$$

where $[x_{\min}, x_{\max}]$, $[y_{\min}, y_{\max}]$, and $[z_{\min}, z_{\max}]$ represent the candidate ranges along the X-, Y- and Z-axes, respectively.

[3]The combination of NOMA and MF-RIS is envisioned as a practically appealing strategy, since NOMA enables flexible and efficient resource allocation for MF-RIS assisted multi-user networks by serving multiple users within the same resource block, and in the meanwhile, MF-RIS facilitates the implementation of NOMA by constructing favorable user channels for NOMA. The proposed MF-RIS can also be used to improve the performance of orthogonal multiple access (OMA) networks, such as frequency division multiple access (FDMA) and time division multiple access (TDMA). Although we consider a NOMA network in this paper, the model and algorithm presented can be easily extended to OMA scenarios as well.

To characterize the performance upper bound that can be achieved by MF-RIS, we assume that perfect channel state information of all channels is available. Since the BS and the MF-RIS are usually deployed at relatively high locations, the line-of-sight (LoS) links can be exploited for them. Therefore, similar to existing RIS works [7], [8], we adopt Rician fading for all channels[4]. For instance, the channel matrix $\mathbf{H} \in \mathbb{C}^{M \times N}$ between the BS and the MF-RIS is given by

$$\mathbf{H} = \underbrace{\sqrt{h_0 d_{bs}^{-\kappa_0}}}_{L_{bs}} \underbrace{\left(\sqrt{\frac{\beta_0}{\beta_0+1}} \mathbf{H}^{\mathrm{LoS}} + \sqrt{\frac{1}{\beta_0+1}} \mathbf{H}^{\mathrm{NLoS}} \right)}_{\hat{\mathbf{H}}}, \tag{2}$$

where L_{bs} is the distance-dependent path loss, and $\hat{\mathbf{H}}$ is composed of the array response and small-scale fading. Specifically, h_0 is the path loss at the reference distance of 1 meter (m), d_{bs} is the link distance between the BS and the MF-RIS, and κ_0 is the corresponding path loss exponent. As for the small-scale fading, β_0 is the Rician factor, and $\mathbf{H}^{\mathrm{NLoS}}$ is the non-LoS component that follows independent and identically distributed (i.i.d.) Rayleigh fading. Assuming that the MF-RIS is placed parallel to the $Y\!-\!Z$ plane and its M elements form an $M_y \times M_z = M$ uniform rectangular array, the LoS component $\mathbf{H}^{\mathrm{LoS}}$ is expressed as [32]

$$\begin{aligned}\mathbf{H}^{\mathrm{LoS}} = & \left[1, e^{-j\frac{2\pi}{\lambda}d\sin\varphi_r\sin\vartheta_r}, \cdots, e^{-j\frac{2\pi}{\lambda}(M_z-1)d\sin\varphi_r\sin\vartheta_r}\right]^{\mathrm{T}} \\ & \otimes \left[1, e^{-j\frac{2\pi}{\lambda}d\sin\varphi_r\cos\vartheta_r}, \cdots, e^{-j\frac{2\pi}{\lambda}(M_y-1)d\sin\varphi_r\cos\vartheta_r}\right]^{\mathrm{T}} \\ & \otimes \left[1, e^{-j\frac{2\pi}{\lambda}d\sin\varphi_t\cos\vartheta_t}, \cdots, e^{-j\frac{2\pi}{\lambda}(N-1)d\sin\varphi_t\cos\vartheta_t}\right], \end{aligned} \tag{3}$$

where the operator $\otimes$ denotes the Kronecker product, λ is the carrier wavelength, and d is the antenna separation. Here, φ_r, ϑ_r, φ_t, and ϑ_t represent the vertical and horizontal angle-of-arrivals, and the vertical and horizontal angle-of-departures of this LoS link, respectively.

The channel vectors from the BS to user U_{kj} and from the MF-RIS to user U_{kj}, denoted by $\mathbf{h}_{kj}^{\mathrm{H}} \in \mathbb{C}^{1 \times N}$ and $\mathbf{g}_{kj}^{\mathrm{H}} \in \mathbb{C}^{1 \times M}$, can be generated by a process similar to obtaining $\mathbf{H}$, and are given by

$$\mathbf{h}_{kj} = \underbrace{\sqrt{h_0 d_{bkj}^{-\kappa_1}}}_{L_{bkj}} \underbrace{\left(\sqrt{\frac{\beta_1}{\beta_1+1}} \mathbf{h}_{kj}^{\mathrm{LoS}} + \sqrt{\frac{1}{\beta_1+1}} \mathbf{h}_{kj}^{\mathrm{NLoS}} \right)}_{\hat{\mathbf{h}}_{kj}}, \tag{4a}$$

$$\mathbf{g}_{kj} = \underbrace{\sqrt{h_0 d_{skj}^{-\kappa_2}}}_{L_{skj}} \underbrace{\left(\sqrt{\frac{\beta_2}{\beta_2+1}} \mathbf{g}_{kj}^{\mathrm{LoS}} + \sqrt{\frac{1}{\beta_2+1}} \mathbf{g}_{kj}^{\mathrm{NLoS}} \right)}_{\hat{\mathbf{g}}_{kj}}. \tag{4b}$$

[4]The formulated problem in Section III and the proposed algorithm in Section IV can be easily extended to MF-RIS assisted communication systems with other channel assumptions (e.g., LoS, Rayleigh and Nakagami fading channels) by replacing with the corresponding channel model.

B. MF-RIS-Aided Downlink NOMA

Using the NOMA protocol, the BS transmits the superimposed signal by exploiting multiple beamforming vectors, i.e., $\mathbf{s} = \sum_{k\in\mathcal{K}} \mathbf{f}_k \sum_{j\in\mathcal{J}_k} \sqrt{p_{kj}} s_{kj}$. Here, $\mathbf{f}_k$ is the transmit beamforming vector for direction k, satisfying $\sum_{k\in\mathcal{K}}\|\mathbf{f}_k\|^2 \leq P_{\mathrm{BS}}^{\max}$, where $P_{\mathrm{BS}}^{\max}$ denotes the maximum transmit power of the BS. Moreover, p_{kj} is the power allocation factor of user U_{kj} with $\sum_{j\in\mathcal{J}_k} p_{kj} = 1$, and $s_{kj} \sim \mathcal{CN}(0,1)$ denotes the modulated data symbol, which is independent over k. Therefore, the signal received at user U_{kj} is given by [33]

$$y_{kj} = \underbrace{\bar{\mathbf{h}}_{kj}\mathbf{f}_k\sqrt{p_{kj}}s_{kj}}_{\text{desired signal}} + \underbrace{\bar{\mathbf{h}}_{kj}\mathbf{f}_k\sum\nolimits_{i\in\{\mathcal{J}_k/j\}}\sqrt{p_{ki}}s_{ki}}_{\text{intra-space interference}} + \underbrace{\bar{\mathbf{h}}_{kj}\mathbf{f}_{\bar{k}}\sum\nolimits_{i\in\mathcal{J}_{\bar{k}}}\sqrt{p_{\bar{k}i}}s_{\bar{k}i}}_{\text{inter-space interference}} + \underbrace{\mathbf{g}_{kj}^{\mathrm{H}}\mathbf{\Theta}_k\mathbf{n}_s}_{\text{RIS noise}} + n_{kj}, \quad (5)$$

where $\bar{k} = r$, if $k = t$; and $\bar{k} = t$, if $k = r$. Moreover, $\mathbf{n}_s \sim \mathcal{CN}(\mathbf{0}, \sigma_s^2\mathbf{I}_M)$ denotes the amplification noise introduced at the MF-RIS with per-element noise power σ_s^2, and $n_{kj} \sim \mathcal{CN}(0, \sigma_u^2)$ denotes the additive white Gaussian noise (AWGN) at user U_{kj} with power σ_u^2. In addition, $\bar{\mathbf{h}}_{kj} = \mathbf{h}_{kj}^{\mathrm{H}} + \mathbf{g}_{kj}^{\mathrm{H}}\mathbf{\Theta}_k\mathbf{H}$ represents the combined channel vector from the BS to user U_{kj}. For conventional passive RISs, the term $\mathbf{g}_{kj}^{\mathrm{H}}\mathbf{\Theta}_k\mathbf{n}_s$ is negligibly small compared to the AWGN at user U_{kj} and thus usually omitted. However, such noise is amplified by the amplification unit in our considered MF-RIS and thus can no longer be ignored.

Following the NOMA protocol, all users employ successive interference cancellation (SIC) to detect the signal and remove interference [4]. We assume that the users in direction k are ranked in an ascending order according to the equivalent combined channel gains, expressed as

$$\frac{|\bar{\mathbf{h}}_{kj}\mathbf{f}_k|^2 p_{kj}}{|\bar{\mathbf{h}}_{kj}\mathbf{f}_k|^2 P_{kj} + |\bar{\mathbf{h}}_{kj}\mathbf{f}_{\bar{k}}|^2 + \sigma_s^2\|\mathbf{g}_{kj}^{\mathrm{H}}\mathbf{\Theta}_k\|^2 + \sigma_u^2} \leq \frac{|\bar{\mathbf{h}}_{kl}\mathbf{f}_k|^2 p_{kj}}{|\bar{\mathbf{h}}_{kl}\mathbf{f}_k|^2 P_{kj} + |\bar{\mathbf{h}}_{kl}\mathbf{f}_{\bar{k}}|^2 + \sigma_s^2\|\mathbf{g}_{kl}^{\mathrm{H}}\mathbf{\Theta}_k\|^2 + \sigma_u^2}, \quad (6)$$

where $k \in \mathcal{K}$, $j \in \mathcal{J}_k$, $l \in \mathcal{L}_k = \{j, j+1, \cdots, J_k\}$, and $P_{kj} = \sum_{i=j+1}^{J_k} p_{ki}$. The SIC condition in (6) can be equivalently transformed into the following inequality:

$$\begin{aligned} &|\bar{\mathbf{h}}_{kj}\mathbf{f}_k|^2 p_{kj}(|\bar{\mathbf{h}}_{kl}\mathbf{f}_k|^2 P_{kj} + |\bar{\mathbf{h}}_{kl}\mathbf{f}_{\bar{k}}|^2 + \sigma_s^2\|\mathbf{g}_{kl}^{\mathrm{H}}\mathbf{\Theta}_k\|^2 + \sigma_u^2) \\ &\leq |\bar{\mathbf{h}}_{kl}\mathbf{f}_k|^2 p_{kj}(|\bar{\mathbf{h}}_{kj}\mathbf{f}_k|^2 P_{kj} + |\bar{\mathbf{h}}_{kj}\mathbf{f}_{\bar{k}}|^2 + \sigma_s^2\|\mathbf{g}_{kj}^{\mathrm{H}}\mathbf{\Theta}_k\|^2 + \sigma_u^2). \end{aligned} \quad (7)$$

By subtracting the term $p_{kj}|\bar{\mathbf{h}}_{kj}\mathbf{f}_k|^2|\bar{\mathbf{h}}_{kl}\mathbf{f}_k|^2 P_{kj}$ from both sides of (7), dividing both sides by p_{kj}, and performing equivalent transformation, we obtain the following inequality:

$$\frac{|\bar{\mathbf{h}}_{kj}\mathbf{f}_k|^2}{|\bar{\mathbf{h}}_{kj}\mathbf{f}_{\bar{k}}|^2 + \sigma_s^2\|\mathbf{g}_{kj}^{\mathrm{H}}\mathbf{\Theta}_k\|^2 + \sigma_u^2} \leq \frac{|\bar{\mathbf{h}}_{kl}\mathbf{f}_k|^2}{|\bar{\mathbf{h}}_{kl}\mathbf{f}_{\bar{k}}|^2 + \sigma_s^2\|\mathbf{g}_{kl}^{\mathrm{H}}\mathbf{\Theta}_k\|^2 + \sigma_u^2}, \ \forall k \in \mathcal{K}, \forall j \in \mathcal{J}_k, \forall l \in \mathcal{L}_k. \quad (8)$$

It can be observed from the above inequality (8) that the SIC condition is independent of the power allocation coefficients $\{p_{kj}\}$.

Based on the SIC condition in (8), for any users U_{kj} and U_{kl} satisfying $j \leq l$, the achievable rate for user U_{kl} to decode the intended signal of user U_{kj} is given by

$$R_{l\to j}^{k} = \log_2\left(1 + \frac{|\bar{\mathbf{h}}_{kl}\mathbf{f}_k|^2 p_{kj}}{|\bar{\mathbf{h}}_{kl}\mathbf{f}_k|^2 P_{kj} + |\bar{\mathbf{h}}_{kl}\mathbf{f}_{\bar{k}}|^2 + \sigma_s^2\|\mathbf{g}_{kl}^{\mathrm{H}}\mathbf{\Theta}_k\|^2 + \sigma_u^2}\right). \tag{9}$$

To guarantee the success of SIC, the achievable signal-to-interference-plus-noise ratio (SINR) at user U_{kl} to decode the signal of user U_{kj} for all $j \leq l$ should be no less than the SINR at user U_{kj} to decode its own signal. Thus, we have the following SIC decoding rate constraint:

$$R_{l\to j}^{k} \geq R_{j\to j}^{k},\ \forall k \in \mathcal{K}, \forall j \in \mathcal{J}_k, \forall l \in \mathcal{L}_k. \tag{10}$$

C. Power Dissipation Model

Define the energy harvesting coefficient matrix of the m-th element as $\mathbf{T}_m = \mathrm{diag}([\underbrace{0, \cdots,}_{1 \text{ to } m-1} 1-\alpha_m \underbrace{, \cdots, 0}_{m+1 \text{ to } M}])$. Then, the RF power received at the m-th element is expressed as

$$P_m^{\mathrm{RF}} = \mathbb{E}\left(\|\mathbf{T}_m\left(\mathbf{H}\mathbf{s} + \mathbf{n}_s\right)\|^2\right), \tag{11}$$

where the expectation operator $\mathbb{E}(\cdot)$ is over $\mathbf{s}$ and $\mathbf{n}_s$.

In order to capture the dynamics of the RF energy conversion efficiency for different input power levels, a non-linear energy harvesting model is adopted in this paper [34]. Accordingly, the total power harvested at the m-th element is given by

$$P_m^{\mathrm{A}} = \frac{\Upsilon_m - Z\Omega}{1-\Omega}, \quad \Upsilon_m = \frac{Z}{1 + e^{-a(P_m^{\mathrm{RF}} - q)}}, \quad \Omega = \frac{1}{1+e^{aq}}, \tag{12}$$

where Υ_m is a logistic function with respect to (w.r.t.) the received RF power P_m^{RF}, and $Z \geq 0$ is a constant determining the maximum harvested power. Constant Ω is introduced to ensure a zero-input/zero-output response for H mode, with constants $a > 0$ and $q > 0$ capturing the joint effects of circuit sensitivity limitations and current leakage.

To ensure the energy self-sustainability, the power consumed by the proposed MF-RIS should not exceed the power harvested. The power consumption of MF-RIS is mainly caused by the operation of reflective and refractive phase shifters, amplifiers, power conversion circuits, and the output power of MF-RIS. Other sources of power consumption, such as powering the impedance matching and mode switching circuits, are negligible in comparison [19]–[21]. Given that the MF-RIS has $2\sum_{m\in\mathcal{M}}\alpha_m$ phase shifters, $2\sum_{m\in\mathcal{M}}\alpha_m$ amplifiers, and $M - \sum_{m\in\mathcal{M}}\alpha_m$ power conversion circuits in operation, we have the following energy self-sustainability constraint:

$$2\left(P_b + P_{\mathrm{DC}}\right)\sum\nolimits_{m\in\mathcal{M}}\alpha_m + (M - \sum\nolimits_{m\in\mathcal{M}}\alpha_m)P_{\mathrm{C}} + \xi P_{\mathrm{O}} \leq \sum\nolimits_{m\in\mathcal{M}} P_m^{\mathrm{A}}, \tag{13}$$

where P_b, $P_{\rm DC}$, and $P_{\rm C}$ denote the power consumed by each phase shifter, the DC biasing power consumed by the amplifier, and the power consumed by the RF-to-DC power conversion circuit, respectively. Here, ξ is the inverse of the amplifier efficiency, and $P_{\rm O}=\sum_{k\in\mathcal{K}}\big(\sum_{k'\in\mathcal{K}}\|\mathbf{\Theta}_k\mathbf{H}\mathbf{f}_{k'}\|^2 +\sigma_s^2\|\mathbf{\Theta}_k\|_F^2\big)$ represents the output power of the MF-RIS.

D. Problem Formulation

Our goal is to maximize the sum-rate of all users while maintaining the self-sustainability of the MF-RIS by jointly optimizing the power allocation, the transmit beamforming at the BS, the coefficient matrix and 3D location of the MF-RIS. The optimization problem is formulated as

$$\max_{p_{kj},\mathbf{f}_k,\mathbf{\Theta}_k,\mathbf{w}} \quad \sum\nolimits_{k\in\mathcal{K}}\sum\nolimits_{j\in\mathcal{J}_k} R_{j\to j}^k \tag{14a}$$

$$\text{s.t.} \quad \sum\nolimits_{j\in\mathcal{J}_k} p_{kj}=1,\ \forall k\in\mathcal{K}, \tag{14b}$$

$$\sum\nolimits_{k\in\mathcal{K}}\|\mathbf{f}_k\|^2\leq P_{\rm BS}^{\max}, \tag{14c}$$

$$R_{j\to j}^k\geq R_{kj}^{\min},\ \forall k\in\mathcal{K},\forall j\in\mathcal{J}_k, \tag{14d}$$

$$\mathbf{\Theta}_k\in\mathcal{R}_{\rm MF},\ \forall k\in\mathcal{K}, \tag{14e}$$

$$(1),(8),(10),(13), \tag{14f}$$

where $\mathcal{R}_{\rm MF}$ denotes the feasible set for the MF-RIS coefficients, with $\mathcal{R}_{\rm MF}=\{\alpha_m,\beta_m^k,\theta_m^k|\alpha_m\in\{0,1\},\beta_m^k\in[0,\beta_{\max}],\sum_{k\in\mathcal{K}}\beta_m^k\leq\beta_{\max},\theta_m^k\in[0,2\pi),\forall m,k\}$. Constraint (14b) represents the power allocation restriction, (14c) ensures that the total transmit power at the BS cannot exceed the power budget $P_{\rm BS}^{\max}$, and (14d) guarantees that the achievable data rate of user U_{kj} is above the quality-of-service (QoS) requirement $R_{kj}^{\min}$. Constraints (14e) and (1) specify the allowable ranges of MF-RIS coefficients and locations, respectively, and (8) determines the SIC decoding order of NOMA users. In addition, constraint (10) ensures successful SIC decoding, and (13) guarantees the energy self-sustainability of the MF-RIS.

The sum-rate maximization problems studied in existing works on self-sustainable RIS [20] and STAR-RIS [33] can be regarded as special cases of problem (14). However, their results are not applicable to solving (14) due to the following new challenges introduced by MF-RIS: 1) the objective function (14a) and constraints (8), (10), (13), and (14d) involve more closely coupled variables; 2) the adopted non-linear energy harvesting model makes constraint (13) more intractable, compared to the linear model in [20]; 3) due to the signal amplification, additional RIS noise needs to be considered in the objective function (14a) and constraints (8), (10), (13), and (14d), which complicates the resource allocation problem; 4) the binary energy harvesting

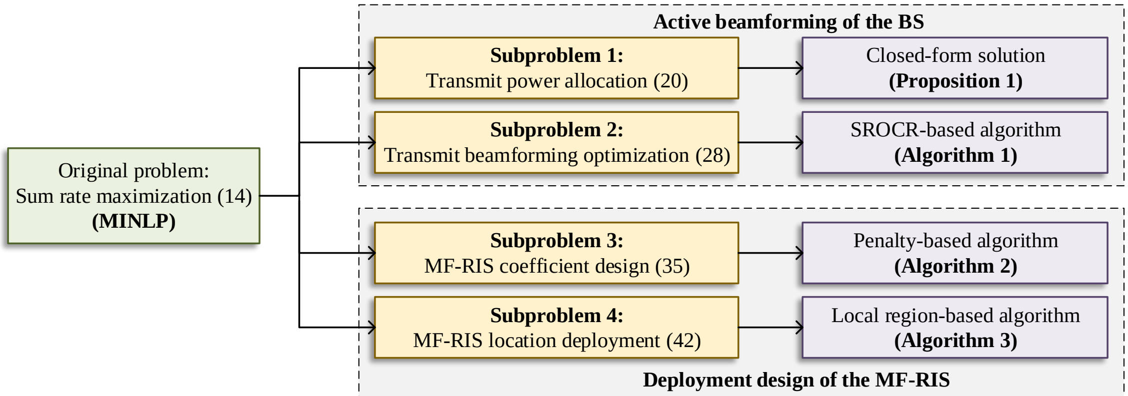

Fig. 2. A roadmap for problem decomposition and algorithm design.

coefficients result in combinatorial constraints (8), (10), (13), (14d), and (14e), which makes (14) an MINLP problem. Therefore, the formulated problem (14) for the MF-RIS is more challenging to solve as compared to those for existing RISs in [20] and [33].

IV. Proposed Solution for Active Beamforming and MF-RIS Deployment

To solve problem (14) efficiently, we propose an AO-based algorithm to obtain a high-performance solution with low complexity. As shown in Fig. 2, the original problem (14) is decomposed into four subproblems, which are tackled one-by-one. Specifically, the optimal power allocation strategy is obtained in closed form based on the successive cancellation. The transmit beamforming optimization is then solved using the sequential rank-one constraint relaxation (SROCR) method. Next, the MF-RIS coefficient is designed by applying the penalty function. Finally, the MF-RIS location is determined by adopting the local region optimization.

A. Problem Transformation

Before solving the original problem (14), we transform it into a more tractable form. First, we observe that constraint (10) is a necessary condition for inequality (8), as (8) is equivalent to inequality (6). This observation shows that under the proposed decoding order, the SIC condition is guaranteed, which is consistent with the conclusions obtained in existing NOMA works such as [33] and [35]. As a result, removing constraint (10) does not affect the optimality of problem (14) when (8) exists. Hence, (10) is removed from problem (14) in the following.

Next, to deal with the non-convex constraint (8), we introduce slack variables A_{kj}, B_{kj}, and Γ_{kj}, and define them as $A_{kj}^{-1}=|\bar{\mathbf{h}}_{kj}\mathbf{f}_k|^2$, $B_{kj}=|\bar{\mathbf{h}}_{kj}\mathbf{f}_{\bar{k}}|^2+\sigma_s^2\|\mathbf{g}_{kj}^{\mathrm{H}}\mathbf{\Theta}_k\|^2+\sigma_u^2$, and $\Gamma_{kj}=A_{kj}^{-1}B_{kj}^{-1}$, respectively. Then, constraint (8) is equivalently transformed into

$$A_{kj}^{-1}\le|\bar{\mathbf{h}}_{kj}\mathbf{f}_k|^2,\ B_{kj}\ge|\bar{\mathbf{h}}_{kj}\mathbf{f}_{\bar{k}}|^2+\sigma_s^2\|\mathbf{g}_{kj}^{\mathrm{H}}\mathbf{\Theta}_k\|^2+\sigma_u^2,\ \Gamma_{kj}\ge A_{kj}^{-1}B_{kj}^{-1},\ \forall k\in\mathcal{K},\forall j\in\mathcal{J}_k, \quad (15a)$$

$$\Gamma_{kj} \leq A_{kl}^{-1} B_{kl}^{-1},\ \forall k \in \mathcal{K}, \forall j \in \mathcal{J}_k, \forall l \in \mathcal{L}_k. \tag{15b}$$

As for the energy self-sustainability constraint (13), it is difficult to directly observe and handle due to the non-linear energy harvesting model based on the logistic function. Therefore, we first substitute the terms in (12) into (13), and equivalently rewrite (13) as the following form:

$$(\mathcal{W} + \xi P_{\rm O})(1 - \Omega) Z^{-1} + M\Omega \leq \sum\nolimits_{m \in \mathcal{M}} \left(1 + \exp(-a(P_m^{\rm RF} - q))\right)^{-1}, \tag{16}$$

where $\mathcal{W} = 2(P_b + P_{\rm DC}) \sum_{m \in \mathcal{M}} \alpha_m + (M - \sum_{m \in \mathcal{M}} \alpha_m) P_{\rm C}$. The complex right-hand-side (RHS) of (16) and the non-convex expression in (11) make (16) difficult to deal with. By introducing slack variables $\zeta_m = P_m^{\rm RF}$ and $\mathcal{C}_m = 1 + \exp(-a(\zeta_m - q))$, we further recast (16) as

$$(\mathcal{W} + \xi P_{\rm O})(1 - \Omega) Z^{-1} + M\Omega \leq \sum\nolimits_{m \in \mathcal{M}} \mathcal{C}_m^{-1}, \tag{17a}$$

$$\zeta_m \leq P_m^{\rm RF},\quad \mathcal{C}_m \geq 1 + \exp\big(-a(\zeta_m - q)\big),\ \forall m. \tag{17b}$$

Constraints (15b) and (17a) are non-convex due to their RHSs. Here, we exploit the successive convex approximation (SCA) technique to tackle them. Specifically, the lower bounds of their RHSs at the feasible point $\{A_{kl}^{(\ell)}, B_{kl}^{(\ell)}, \mathcal{C}_m^{(\ell)}\}$ in the ℓ-th iteration are, respectively, given by

$$\Gamma_{kl}^{\rm lb} = \frac{1}{A_{kl}^{(\ell)} B_{kl}^{(\ell)}} - \frac{A_{kl} - A_{kl}^{(\ell)}}{(A_{kl}^{(\ell)})^2 B_{kl}^{(\ell)}} - \frac{B_{kl} - B_{kl}^{(\ell)}}{(B_{kl}^{(\ell)})^2 A_{kl}^{(\ell)}},\quad \mathcal{C}^{\rm lb} = \sum\nolimits_{m \in \mathcal{M}} \left(\frac{2}{\mathcal{C}_m^{(\ell)}} - \frac{\mathcal{C}_m}{(\mathcal{C}_m^{(\ell)})^2}\right). \tag{18}$$

As a result, by defining $\bar{W} = \frac{(\mathcal{C}^{\rm lb} - M\Omega)Z}{(1-\Omega)\xi} - \frac{\mathcal{W}}{\xi}$ and $\Delta_0 = \{A_{kj}, B_{kj}, \Gamma_{kj}, \mathcal{C}_m, \zeta_m\}$, problem (14) is equivalently transformed into the following one:

$$\max_{p_{kj}, \mathbf{f}_k, \mathbf{\Theta}_k, \mathbf{w}, \Delta_0} \sum\nolimits_k \sum\nolimits_{j \in \mathcal{J}_k} R_{j \to j}^k \tag{19a}$$

$$\text{s.t.}\quad \Gamma_{kj} \leq \Gamma_{kl}^{\rm lb},\ \forall k \in \mathcal{K}, \forall j \in \mathcal{J}_k, \forall l \in \mathcal{L}_k, \tag{19b}$$

$$\bar{W} \geq P_{\rm O},\ (1), (14\text{b})\text{-}(14\text{e}), (15\text{a}), (17\text{b}). \tag{19c}$$

B. Power Allocation

To start with, we focus on the optimization of $\{p_{kj}\}$ with given $\{\mathbf{f}_k, \mathbf{\Theta}_k, \mathbf{w}\}$. Since the inter-cluster interference is independent of $\{p_{kj}\}$, the power allocation problem can be decomposed into two subproblems [35]. For direction k, the optimization problem is formulated as

$$\max_{p_{kj}} \quad \sum\nolimits_{j \in \mathcal{J}_k} R_{j \to j}^k \tag{20a}$$

$$\text{s.t.}\quad (14\text{b}), (14\text{d}). \tag{20b}$$

We divide p_{kj} into two parts, $\bar{p}_{kj}$ and $\triangle p_{kj}$, where $p_{kj} = \bar{p}_{kj} + \triangle p_{kj}$, with $\bar{p}_{kj}$ denoting the minimum power allocation coefficient for user U_{kj} to satisfy the QoS constraint (14d) and $\triangle p_{kj}$ denoting the power increment allocated to user U_{kj}. Then, based on the SIC decoding, the optimal power allocation coefficients can be obtained by the following lemma and proposition.

***Lemma** 1: Problem (20) is feasible if the following inequality holds:*

$$\sum\nolimits_{j\in\mathcal{J}_k}\bar{p}_{kj}=\sum\nolimits_{j\in\mathcal{J}_k}\left(\prod\nolimits_{i=1}^{j-1}(r_{ki}^{\min}+1)\right)\frac{r_{kj}^{\min}}{\gamma_{kj}}\leq 1, \tag{21}$$

where

$$r_{kj}^{\min}=2^{R_{kj}^{\min}}-1,\ \prod\nolimits_{i=1}^{0}(r_{kj}^{\min}+1)=1,\ and\ \gamma_{kj}=\frac{|\bar{\mathbf{h}}_{kj}\mathbf{f}_k|^2}{|\bar{\mathbf{h}}_{kj}\mathbf{f}_{\bar{k}}|^2+\sigma_s^2\|\mathbf{g}_{kj}^{\rm H}\boldsymbol{\Theta}_k\|^2+\sigma_u^2}. \tag{22}$$

Proof: See Appendix A. □

***Proposition** 1: If Lemma 1 is satisfied, the optimal power allocation coefficients are given by*

$$p_{kj}^{\star}=\begin{cases}\underbrace{\frac{r_{kj}^{\min}}{\gamma_{kj}}+r_{kj}^{\min}\sum\nolimits_{i=j+1}^{J_k}\bar{p}_{ki}^{\star}}_{\bar{p}_{kj}^{\star}}+\underbrace{r_{kj}^{\min}\sum\nolimits_{i=j+1}^{J_k}\triangle p_{ki}^{\star}}_{\triangle p_{kj}^{\star}}, & j=1,2,\cdots,J_k-1,\\ \underbrace{\frac{r_{kj}^{\min}}{\gamma_{kj}}}_{\bar{p}_{kj}^{\star}}+\underbrace{\frac{1-\sum_{i\in\mathcal{J}_k}\bar{p}_{ki}^{\star}}{\prod_{i=1}^{J_k-1}(1+r_{ki}^{\min})}}_{\triangle p_{kj}^{\star}}, & j=J_k,\end{cases} \tag{23}$$

and the optimal objective value of problem (20) is given by

$$\sum\nolimits_{j\in\mathcal{J}_k}\log_2\left(1+\frac{\bar{p}_{kj}^{\star}+r_{kj}^{\min}\sum_{i=j+1}^{J_k}\triangle p_{ki}^{\star}}{\sum_{i=j+1}^{J_k}p_{ki}^{\star}+\frac{1}{\gamma_{kj}}}\right)+\log_2\left(1+\frac{(1-\sum_{j\in\mathcal{J}_k}\bar{p}_{kj}^{\star})\gamma_{kJ_k}}{\prod_{i=1}^{J_k}(1+r_{ki}^{\min})}\right). \tag{24}$$

Proof: See Appendix B. □

Proposition 1 shows that the optimal power allocation coefficient, $p_{kj}^{\star}$, can be divided into two parts, $\bar{p}_{kj}^{\star}$ and $\triangle p_{kj}^{\star}$, where $p_{kj}^{\star}=\bar{p}_{kj}^{\star}+\triangle p_{kj}^{\star}$. Specifically, $\bar{p}_{kj}^{\star}$ maintains the QoS constraint of user U_{kj}. In addition, $\triangle p_{kJ_k}^{\star}$ maximizes the data rate of user U_{kJ_k}, while for other users, $\triangle p_{kj}^{\star}$ compensates for the SINR loss caused by the SIC interference. This is due to the fact that: 1) the users are ordered according to their equivalent channel gains; 2) at the optimum, improving the rate of one user comes at the cost of decreasing the rate of other users.

C. Transmit Beamforming Optimization

With given $\{p_{kj},\boldsymbol{\Theta}_k,\mathbf{w}\}$, we aim to solve the transmit beamforming vector $\mathbf{f}_k$. Problem (19) is still difficult to solve directly due to the non-concave objective function (19a) and the non-convex constraint (14d). To this end, we introduce auxiliary variables Q_{kj} and C_{kj}, satisfying $Q_{kj}=R_{j\to j}^{k}$ and $C_{kj}=|\bar{\mathbf{h}}_{kj}\mathbf{f}_k|^2P_{kj}+B_{kj}$. The objective function (14a) is then transformed into

$$\sum\nolimits_{k\in\mathcal{K}}\sum\nolimits_{j\in\mathcal{J}_k}R_{j\to j}^{k}=\sum\nolimits_{k\in\mathcal{K}}\sum\nolimits_{j\in\mathcal{J}_k}Q_{kj}. \tag{25}$$

In addition, we obtain the following new constraints:

$$C_{kj}\geq|\mathbf{h}_{kj}\mathbf{f}_k|^2P_{kj}+B_{kj},\quad Q_{kj}\leq\log_2\left(1+p_{kj}A_{kj}^{-1}C_{kj}^{-1}\right),\quad Q_{kj}\geq R_{kj}^{\min}. \tag{26}$$

The SCA technique is employed to handle the non-convex constraint $Q_{kj}\leq\log_2\left(1+p_{kj}A_{kj}^{-1}C_{kj}^{-1}\right)$.

Specifically, a lower bound of its RHS in the ℓ-th iteration is expressed as

$$R_{kj}^{\mathrm{lb}} = \log_2\left(1+\frac{p_{kj}}{A_{kj}^{(\ell)}C_{kj}^{(\ell)}}\right) - \frac{p_{kj}(\log_2 e)(A_{kj}-A_{kj}^{(\ell)})}{p_{kj}A_{kj}^{(\ell)}+(A_{kj}^{(\ell)})^2C_{kj}^{(\ell)}} - \frac{p_{kj}(\log_2 e)(C_{kj}-C_{kj}^{(\ell)})}{p_{kj}C_{kj}^{(\ell)}+(C_{kj}^{(\ell)})^2A_{kj}^{(\ell)}}. \tag{27}$$

Substituting (25)-(27) into (19), the transmit beamforming optimization problem is written as

$$\max_{\mathbf{f}_k,\Delta_1} \sum\nolimits_k \sum\nolimits_{j\in\mathcal{J}_k} Q_{kj} \tag{28a}$$

$$\mathrm{s.t.}\ \ A_{kj}^{-1} \le |\bar{\mathbf{h}}_{kj}\mathbf{f}_k|^2,\ B_{kj} \ge |\bar{\mathbf{h}}_{kj}\mathbf{f}_{\bar{k}}|^2 + \sigma_s^2\|\mathbf{g}_{kj}^{\mathrm{H}}\mathbf{\Theta}_k\|^2 + \sigma_u^2,\ \forall k\in\mathcal{K},\forall j\in\mathcal{J}_k, \tag{28b}$$

$$C_{kj} \ge |\mathbf{h}_{kj}\mathbf{f}_k|^2 P_{kj} + B_{kj},\ \forall k\in\mathcal{K},\forall j\in\mathcal{J}_k, \tag{28c}$$

$$\Gamma_{kj} \ge A_{kj}^{-1}B_{kj}^{-1},\ \Gamma_{kj}\le \Gamma_{kl}^{\mathrm{lb}},\ Q_{kj}\le R_{kj}^{\mathrm{lb}},\ Q_{kj}\ge R_{kj}^{\min},\ \forall k\in\mathcal{K},\forall j\in\mathcal{J}_k,\forall l\in\mathcal{L}_k, \tag{28d}$$

$$\mathcal{C}_m \ge 1+\exp\left(-a\left(\zeta_m - q\right)\right),\ \forall m, \tag{28e}$$

$$\bar{W} \ge P_{\mathrm{O}},\ \zeta_m \le P_m^{\mathrm{RF}},\ \forall m,\ (14\mathrm{c}), \tag{28f}$$

where $\Delta_1 = \{A_{kj}, B_{kj}, C_{kj}, Q_{kj}, \Gamma_{kj}, \mathcal{C}_m, \zeta_m\}$. We define $\bar{\mathbf{H}}_{kj} = \bar{\mathbf{h}}_{kj}^{\mathrm{H}}\bar{\mathbf{h}}_{kj}$ and $\mathbf{F}_k = \mathbf{f}_k\mathbf{f}_k^{\mathrm{H}}$, satisfying $\mathbf{F}_k \succeq \mathbf{0}$ and $\mathrm{rank}(\mathbf{F}_k)=1$. Then, problem (28) is equivalently transformed into

$$\max_{\mathbf{F}_k,\Delta_1} \sum\nolimits_{k\in\mathcal{K}} \sum\nolimits_{j\in\mathcal{J}_k} Q_{kj} \tag{29a}$$

$$\mathrm{s.t.}\ \ A_{kj}^{-1} \le \mathrm{Tr}\left(\bar{\mathbf{H}}_{kj}\mathbf{F}_k\right),\ B_{kj} \ge \mathrm{Tr}\left(\bar{\mathbf{H}}_{kj}\mathbf{F}_{\bar{k}}\right) + \sigma_s^2\|\mathbf{g}_{kj}^{\mathrm{H}}\mathbf{\Theta}_k\|^2 + \sigma_u^2,\ \forall k\in\mathcal{K},\forall j\in\mathcal{J}_k, \tag{29b}$$

$$C_{kj} \ge \mathrm{Tr}\left(\bar{\mathbf{H}}_{kj}\mathbf{F}_k\right)P_{kj} + B_{kj},\ \forall k\in\mathcal{K},\forall j\in\mathcal{J}_k, \tag{29c}$$

$$\bar{W} \ge \sum\nolimits_{k\in\mathcal{K}}\left(\sum\nolimits_{k'\in\mathcal{K}} \mathrm{Tr}\left(\mathbf{\Theta}_k\mathbf{H}\mathbf{F}_{k'}\mathbf{H}^{\mathrm{H}}\mathbf{\Theta}_k^{\mathrm{H}}\right) + \sigma_s^2\|\mathbf{\Theta}_k\|_F^2\right), \tag{29d}$$

$$\zeta_m \le \sum\nolimits_{k\in\mathcal{K}} \mathrm{Tr}\left(\bar{\mathbf{T}}_m\mathbf{H}\mathbf{F}_k\mathbf{H}^{\mathrm{H}}\bar{\mathbf{T}}_m^{\mathrm{H}}\right)(1-\alpha_m) + \sigma_s^2(1-\alpha_m),\ \forall m, \tag{29e}$$

$$\mathrm{rank}(\mathbf{F}_k) = 1,\ \forall k, \tag{29f}$$

$$\sum\nolimits_{k\in\mathcal{K}} \mathrm{Tr}\left(\mathbf{F}_k\right) \le P_{\mathrm{BS}}^{\max},\ \mathbf{F}_k \succeq 0,\ \forall k,\ (28\mathrm{d}),(28\mathrm{e}), \tag{29g}$$

where $\bar{\mathbf{T}}_m = \mathrm{diag}([\underbrace{0,\cdots,}_{1\text{ to }m-1}1\underbrace{,\cdots,0}_{m+1\text{ to }M}])$.

Next, we adopt the sequential rank-one constraint relaxation (SROCR) method to handle the rank-one constraint (29f). Different from the conventional semidefinite relaxation (SDR) method that drops the rank-one constraint directly [36], the basic idea of SROCR is to relax the rank-one constraint gradually to obtain a feasible rank-one solution [37]. Specifically, we define $w_k^{(\ell-1)} \in [0,1]$ as the trace ratio parameter of $\mathbf{F}_k$ in the $(\ell-1)$-th iteration. Then, constraint (29f) in the ℓ-th iteration is replaced by the following linear one:

$$\left(\mathbf{f}_k^{\mathrm{e},(\ell-1)}\right)^{\mathrm{H}}\mathbf{F}_k^{(\ell)}\mathbf{f}_k^{\mathrm{e},(\ell-1)} \ge w_k^{(\ell-1)}\mathrm{Tr}(\mathbf{F}_k^{(\ell)}),\ \forall k, \tag{30}$$

Algorithm 1 The SROCR-Based Algorithm for Solving Problem (29)

Initialize feasible points $\{\mathbf{F}_k^{(0)}, w_k^{(0)}\}$ and the step size $\delta_1^{(0)}$. Set the iteration index $\ell_1 = 0$.
repeat
  if problem (31) is solvable **then**
    Update $\mathbf{F}_k^{(\ell_1+1)}$ by solving problem (31); Update $\delta_1^{(\ell_1+1)} = \delta_1^{(\ell_1)}$;
  else
    Update $\delta_1^{(\ell_1+1)} = \frac{\delta_1^{(\ell_1)}}{2}$;
  end if
  Update $w_k^{(\ell_1+1)} = \min\left(1, \frac{\lambda_{\max}(\mathbf{F}_k^{(\ell_1+1)})}{\mathrm{Tr}(\mathbf{F}_k^{(\ell_1+1)})} + \delta_1^{(\ell_1+1)}\right)$; Update $\ell_1 = \ell_1 + 1$;
until the stopping criterion is met.

where $\mathbf{f}_k^{\mathrm{e},(\ell-1)}$ is the eigenvector corresponding to the largest eigenvalue of $\mathbf{F}_k^{(\ell-1)}$, and $\mathbf{F}_k^{(\ell-1)}$ is the solution in the $(\ell-1)$-th iteration with given $w_k^{(\ell-1)}$. Therefore, problem (29) is recast as

$$\max_{\mathbf{F}_k, \Delta_1} \quad \sum\nolimits_{k\in\mathcal{K}} \sum\nolimits_{j\in\mathcal{J}_k} Q_{kj} \tag{31a}$$

$$\mathrm{s.t.} \quad (29\mathrm{b})\text{-}(29\mathrm{e}), (29\mathrm{g}), (30). \tag{31b}$$

Problem (31) is a convex semi-definite programming (SDP) problem, which can be solved efficiently via CVX [38]. By increasing $w_k^{(\ell-1)}$ from 0 to 1 over iterations, we approach a rank-one solution gradually. The iterative algorithm for solving (29) is given in Algorithm 1. After solving (29), the solution of $\mathbf{f}_k$ is obtained by Cholesky decomposition of $\mathbf{F}_k$, e.g., $\mathbf{F}_k = \mathbf{f}_k \mathbf{f}_k^{\mathrm{H}}$.

D. MF-RIS Coefficient Deign

For any given $\{p_{kj}, \mathbf{f}_k, \mathbf{w}\}$, we define $\mathbf{U}_k = \mathbf{u}_k \mathbf{u}_k^{\mathrm{H}}$ and $\mathbf{u}_k = [\alpha_1 \sqrt{\beta_1^k} e^{-j\theta_1^k}; \cdots; \alpha_M \sqrt{\beta_M^k} e^{-j\theta_M^k}; 1]$, satisfying $\mathbf{U}_k \succeq \mathbf{0}$, $\mathrm{rank}(\mathbf{U}_k) = 1$, $[\mathbf{U}_k]_{m,m} = \alpha_m^2 \beta_m^k$, and $[\mathbf{U}_k]_{M+1,M+1} = 1$. Then, we have

$$|\bar{\mathbf{h}}_{kj} \mathbf{f}_{kj}|^2 = \mathrm{Tr}\left(\widetilde{\mathbf{H}}_{kj} \mathbf{F}_k \widetilde{\mathbf{H}}_{kj}^{\mathrm{H}} \mathbf{U}_k\right), \ \|\mathbf{g}_{kj}^{\mathrm{H}} \boldsymbol{\Theta}_k\|^2 = \mathrm{Tr}(\widetilde{\mathbf{G}}_{kj} \mathbf{U}_k), \ P_{\mathrm{O}} = \sum\nolimits_{k\in\mathcal{K}} \mathrm{Tr}(\widetilde{\mathbf{H}} \mathbf{U}_k), \tag{32}$$

where

$$\widetilde{\mathbf{H}}_{kj} = \left[\mathrm{diag}(\mathbf{g}_{kj}^{\mathrm{H}}) \mathbf{H}; \mathbf{h}_{kj}^{\mathrm{H}}\right], \ \widetilde{\mathbf{G}}_{kj} = [\mathrm{diag}(\mathbf{g}_{kj}^{\mathrm{H}}); \mathbf{0}_{1\times M}][\mathrm{diag}(\mathbf{g}_{kj}^{\mathrm{H}}); \mathbf{0}_{1\times M}]^{\mathrm{H}}, \tag{33a}$$

$$\widetilde{\mathbf{H}} = \sum\nolimits_{k'\in\mathcal{K}} [\mathbf{H}\mathbf{f}_{k'}; 0][\mathbf{H}\mathbf{f}_{k'}; 0]^{\mathrm{H}} + \sigma_s^2 [\mathbf{I}_M; \mathbf{0}_{1\times M}][\mathbf{I}_M; \mathbf{0}_{1\times M}]^{\mathrm{H}}. \tag{33b}$$

Constraints (29b)-(29d) are then, respectively, rewritten as

$$A_{kj}^{-1} \leq \mathrm{Tr}(\widetilde{\mathbf{H}}_{kj} \mathbf{F}_k \widetilde{\mathbf{H}}_{kj}^{\mathrm{H}} \mathbf{U}_k), \quad B_{kj} \geq \mathrm{Tr}\big((\widetilde{\mathbf{H}}_{kj} \mathbf{F}_{\bar{k}} \widetilde{\mathbf{H}}_{kj}^{\mathrm{H}} + \sigma_s^2 \widetilde{\mathbf{G}}_{kj}) \mathbf{U}_k\big) + \sigma_u^2, \tag{34a}$$

$$C_{kj} \geq \mathrm{Tr}\big(\widetilde{\mathbf{H}}_{kj} \mathbf{F}_k \widetilde{\mathbf{H}}_{kj}^{\mathrm{H}} \mathbf{U}_k\big) P_{kj} + B_{kj}, \quad \bar{\mathcal{W}} \geq \sum\nolimits_{k\in\mathcal{K}} \mathrm{Tr}(\widetilde{\mathbf{H}} \mathbf{U}_k). \tag{34b}$$

Accordingly, the MF-RIS coefficient design problem is formulated as

$$\max_{\mathbf{U}_k, \Delta_1} \quad \sum\nolimits_{k\in\mathcal{K}} \sum\nolimits_{j\in\mathcal{J}_k} Q_{kj} \tag{35a}$$

$$\mathrm{s.t.} \quad \mathbf{U}_k \succeq 0, \ \ [\mathbf{U}_k]_{M+1,M+1} = 1, \ \forall k, \tag{35b}$$

Algorithm 2 The Penalty-Based Algorithm for Solving Problem (35)

Initialize feasible points $\{\mathbf{U}_k^{(0)}, v_k^{(0)}\}$, $\varepsilon > 1$, and the step size $\delta_2^{(0)}$. Set the iteration index $\ell_2 = 0$ and the maximum value of the penalty factor $\rho_{\max}$.
repeat
  if $\ell_2 \leq \ell_2^{\max}$ **then**
    if problem (38) is solvable **then**
      Update $\mathbf{U}_k^{(\ell_2+1)}$ by solving problem (38); Update $\delta_2^{(\ell_2+1)} = \delta_2^{(\ell_2)}$;
    else
      Update $\delta_2^{(\ell_2+1)} = \frac{\delta_2^{(\ell_2)}}{2}$;
    end if
    Update $v_k^{(\ell_2+1)} = \min\left(1, \frac{\lambda_{\max}(\mathbf{U}_k^{(\ell_2+1)})}{\mathrm{Tr}(\mathbf{U}_k^{(\ell_2+1)})} + \delta_2^{(\ell_2+1)}\right)$;
    Update $\rho^{(\ell_2+1)} = \min\{\varepsilon\rho^{(\ell_2)}, \rho_{\max}\}$; Update $\ell_2 = \ell_2 + 1$;
  else
    Reinitialize with a new $\mathbf{U}_k^{(0)}$, set $\varepsilon > 1$ and $\ell_2 = 0$.
  end if
until the stopping criterion is met.

$$[\mathbf{U}_k]_{m,m} = \alpha_m^2 \beta_m^k, \ \forall m, k, \tag{35c}$$

$$\mathrm{rank}(\mathbf{U}_k) = 1, \ \forall k, \tag{35d}$$

$$\alpha_m \in \{0, 1\}, \ \forall m, \tag{35e}$$

$$\beta_m^k \in [0, \beta_{\max}], \ \sum\nolimits_{k \in \mathcal{K}} \beta_m^k \leq \beta_{\max}, \ \forall m, k, \ (28\text{d}), (28\text{e}), (29\text{e}), (34). \tag{35f}$$

The non-convexity of problem (35) arises from the non-convex constraint (35c), the rank-one constraint (35d), and the binary constraint (35e). In Section IV-C, we showed how to handle the rank-one constraint using SROCR. Similarly, by defining $v_k^{(\ell-1)}$, $\mathbf{u}_k^{\mathrm{e},(\ell-1)}$, and $\mathbf{U}_k^{(\ell)}$ to correspond to $w_k^{(\ell-1)}$, $\mathbf{f}_k^{\mathrm{e},(\ell-1)}$, and $\mathbf{F}_k^{(\ell)}$ in (30), the rank-one constraint (35d) is approximated by

$$\left(\mathbf{u}_k^{\mathrm{e},(\ell-1)}\right)^{\mathrm{H}} \mathbf{U}_k^{(\ell)} \mathbf{u}_k^{\mathrm{e},(\ell-1)} \geq v_k^{(\ell-1)} \mathrm{Tr}(\mathbf{U}_k^{(\ell)}), \ \forall k. \tag{36}$$

The binary constraint (35e) can be equivalently transformed into two continuous constraints: $\alpha_m - \alpha_m^2 \leq 0$ and $0 \leq \alpha_m \leq 1$. However, constraint $\alpha_m - \alpha_m^2 \leq 0$ is still non-convex due to the non-convex term $-\alpha_m^2$. The SCA technique is employed to address it. Specifically, for a given point $\{\alpha_m^{(\ell)}\}$ in the ℓ-th iteration, an upper bound is obtained as $(-\alpha_m^2)^{\mathrm{ub}} = -2\alpha_m^{(\ell)}\alpha_m + (\alpha_m^{(\ell)})^2$.

To address the highly-coupled constraint (35c), the auxiliary variable $\eta_m^k = \alpha_m^2 \beta_m^k$ is introduced so that we can obtain the equivalent form of (35c) as

$$[\mathbf{U}_k]_{m,m} = \eta_m^k, \quad \eta_m^k = \alpha_m^2 \beta_m^k. \tag{37}$$

The non-convex constraint $\eta_m^k = \alpha_m^2 \beta_m^k$ is transformed into the convex penalty term $G(\alpha_m, \beta_m^k, \eta_m^k)$ $= \sum_{k \in \mathcal{K}} \sum_{m \in \mathcal{M}} (\frac{c_m^k}{2} \alpha_m^4 + \frac{(\beta_m^k)^2}{2c_m^k} - \eta_m^k)$ by using the penalty-based method and convex upper bound

(CUB) method, where the fixed point $\{c_m^k\}$ in the ℓ-th iteration is updated by $(c_m^k)^{(\ell)} = \frac{(\beta_m^k)^{(\ell-1)}}{(\alpha_m^{(\ell-1)})^2}$; see Appendix C for the derivation details. Finally, problem (35) is recast as

$$\max_{\mathbf{U}_k,\Delta_1,\eta_m^k} \sum\nolimits_{k\in\mathcal{K}} \sum\nolimits_{j\in\mathcal{J}_k} Q_{kj} - \rho G(\alpha_m, \beta_m^k, \eta_m^k) \tag{38a}$$

$$\text{s.t.}\ \ 0 \le \alpha_m \le 1,\ \alpha_m + \left(-\alpha_m^2\right)^{\text{ub}} \le 0,\ \forall m, \tag{38b}$$

$$[\mathbf{U}_k]_{m,m} = \eta_m^k,\ \forall m, k,\ (35\text{b}), (35\text{f}), (36), \tag{38c}$$

where the penalty factor $\rho > 0$ penalizes the objective function (38a) if $G(\alpha_m, \beta_m^k, \eta_m^k) \neq 0$. It can be verified that, if $\rho \to \infty$, the solution obtained from problem (38) satisfies $G(\alpha_m, \beta_m^k, \eta_m^k) = 0$. Problem (38) is a convex SDP problem, which can be solved efficiently via CVX [38]. The details of the proposed penalty-based algorithm are given in Algorithm 2.

E. MF-RIS Location Optimization

Finally, we focus on the location optimization of the MF-RIS. Equations (2), (3), and (4b) show that both the distance-dependent path loss, L_{bs} and L_{skj}, and the LoS components, $\mathbf{H}^{\text{LoS}}$ and $\mathbf{g}_{kj}^{\text{LoS}}$, are relevant to the MF-RIS location, $\mathbf{w}$. In addition, (3) shows that these LoS components are non-linear w.r.t. $\mathbf{w}$, which are difficult to deal with directly. Here, we invoke the local region optimization method to tackle this issue [8]. Denote $\mathbf{w}^{(i-1)}$ as the feasible location obtained in the $(i-1)$-th iteration, then the location variables should satisfy the following constraint:

$$\left\|\mathbf{w} - \mathbf{w}^{(i-1)}\right\| \le \epsilon, \tag{39}$$

where the constant ϵ is relatively small such that $\mathbf{w}^{(i-1)}$ can be used to approximately obtain $\mathbf{H}^{\text{LoS}}$ and $\mathbf{g}_{kj}^{\text{LoS}}$ in the i-th iteration. Assume $\hat{\mathbf{H}}^{(i-1)}$ and $\hat{\mathbf{g}}_{kj}^{(i-1)}$ are the small-scale fading obtained in the $(i-1)$-th iteration, then constraints (29b)-(29e) are, respectively, rewritten as

$$A_{kj}^{-1} \le \mathbf{d}_{kj}^{\text{T}} \mathbf{D}_{kj} \mathbf{d}_{kj},\quad B_{kj} \ge \mathbf{d}_{kj}^{\text{T}} \bar{\mathbf{D}}_{kj} \mathbf{d}_{kj} + d_{skj}^{-\kappa_2} \mathcal{W}_1 + \sigma_u^2, \tag{40a}$$

$$C_{kj} \ge \mathbf{d}_{kj}^{\text{T}} \mathbf{D}_{kj} \mathbf{d}_{kj} P_{kj} + B_{kj},\quad d_{bs}^{-\kappa_0} \le \mathcal{W}_2,\quad d_{bs}^{-\kappa_0} \ge \mathcal{W}_3, \tag{40b}$$

where $\mathbf{d}_{kj} = \left[1, d_{bs}^{-\frac{\kappa_0}{2}} d_{skj}^{-\frac{\kappa_2}{2}}\right]^{\text{T}}$. Here, $\mathbf{D}_{kj}$, $\bar{\mathbf{D}}_{kj}$, $\mathcal{W}_1$, $\mathcal{W}_2$, and $\mathcal{W}_3$ are terms unrelated to the optimization variable $\mathbf{w}$ in the i-th iteration, which are given by (41) at the bottom of the next page. Accordingly, given $\{p_{kj}, \mathbf{f}_k, \mathbf{\Theta}_k\}$, problem (19) is reduced to

$$\max_{\mathbf{w},\Delta_1} \sum\nolimits_{k\in\mathcal{K}} \sum\nolimits_{j\in\mathcal{J}_k} Q_{kj} \tag{42a}$$

$$\text{s.t.}\ \ (1), (28\text{d}), (28\text{e}), (39), (40\text{a}), (40\text{b}). \tag{42b}$$

Constraints (40a) and (40b) are still non-convex w.r.t. $\mathbf{w}$. To tackle this issue, we first introduce auxiliary variables to replace their complex terms, and then approximate the non-convex parts by

Algorithm 3 The Local Region-Based Algorithm for Solving Problem (42)

1: Initialize feasible points $\{x^{(0)}, y^{(0)}, z^{(0)}, t^{(0)}, t_{kj}^{(0)}, \bar{v}^{(0)}\}$. Set the iteration index $\ell_3 = 0$.
2: **repeat**
3: Update $\{x^{(\ell_3+1)}, y^{(\ell_3+1)}, z^{(\ell_3+1)}, t^{(\ell_3+1)}, t_{kj}^{(\ell_3+1)}, \bar{v}^{(\ell_3+1)}\}$ by solving problem (44);
4: Update $\ell_3 = \ell_3 + 1$;
5: **until** the stopping criterion is met.

using SCA. Specifically, by introducing a slack variable set $\Delta_2 = \{t, t_{kj}, \bar{t}_{kj}, e_{kj}, v, \bar{v}, r_{kj}, \bar{r}_{kj}, s_{kj}\}$ and defining $\bar{\mathbf{d}}_{kj} = [1, \bar{t}_{kj}]^{\mathrm{T}}$, constraints (40a) and (40b) are linearly approximated by

$$r_{kj} \leq -(\bar{\mathbf{d}}_{kj}^{(\ell)})^{\mathrm{T}} \mathbf{D}_{kj} \bar{\mathbf{d}}_{kj}^{(\ell)} + 2\Re\big((\bar{\mathbf{d}}_{kj}^{(\ell)})^{\mathrm{T}} \mathbf{D}_{kj} \bar{\mathbf{d}}_{kj}\big),\ \bar{r}_{kj} \geq \bar{\mathbf{d}}_{kj}^{\mathrm{T}} \mathbf{D}_{kj} \bar{\mathbf{d}}_{kj},\ s_{kj} \geq \bar{\mathbf{d}}_{kj}^{\mathrm{T}} \bar{\mathbf{D}}_{kj} \bar{\mathbf{d}}_{kj}, \tag{43a}$$

$$A_{kj}^{-1} \leq r_{kj},\ B_{kj} \geq s_{kj} + e_{kj}\mathcal{W}_1 + \sigma_u^2,\ C_{kj} \geq \bar{r}_{kj} P_{kj} + B_{kj},\ v \leq \mathcal{W}_2,\ \bar{v} \geq \mathcal{W}_3,\ \bar{t}_{kj} \leq t t_{kj}, \tag{43b}$$

$$x^2 + x_b^2 + y^2 + y_b^2 + z^2 + z_b^2 - 2x_b x - 2y_b y - 2z_b z + f(t, -\frac{4}{\kappa_0}) \leq 0, \tag{43c}$$

$$x^2 + x_{kj}^2 + y^2 + y_{kj}^2 + z^2 - 2x_{kj} x - 2y_{kj} y + f(t_{kj}, -\frac{4}{\kappa_2}) \leq 0, \tag{43d}$$

$$f(x,2) - x_{kj}^2 + f(y,2) - y_{kj}^2 + f(z,2) + 2x_{kj} x + 2y_{kj} y + e_{kj}^{-\frac{2}{\kappa_2}} \leq 0, \tag{43e}$$

$$f(x,2) - x_b^2 + f(y,2) - y_b^2 + f(z,2) - z_b^2 + 2x_b x + 2y_b y + 2z_b z + v^{-\frac{2}{\kappa_0}} \leq 0, \tag{43f}$$

$$x^2 + x_b^2 + y^2 + y_b^2 + z^2 + z_b^2 - 2x_b x - 2y_b y - 2z_b z + f(\bar{v}, -\frac{2}{\kappa_0}) \leq 0, \tag{43g}$$

where the function $f(p,q) = -(p^{(\ell)})^q - q(p^{(\ell)})^{q-1}(p - p^{(\ell)})$ is the first-order Taylor expansion of $-p^q$ at the given point $\{p^{(\ell)}\}$. The proof of (43) is given in Appendix D.

Next, reformulating problem (42) by replacing constraints (40a) and (40b) with the convex ones (43a)-(43g) yields the following optimization problem:

$$\max_{\mathbf{w}, \Delta_1, \Delta_2} \quad \sum\nolimits_{k \in \mathcal{K}} \sum\nolimits_{j \in \mathcal{J}_k} Q_{kj} \tag{44a}$$

$$\text{s.t.} \quad (1), (28\text{d}), (28\text{e}), (39), (43\text{a})\text{-}(43\text{g}). \tag{44b}$$

Problem (44) is convex, which can be solved efficiently via CVX [38]. The details of the proposed local region-based algorithm are given in Algorithm 3.

$$\mathbf{D}_{kj} = \mathbf{E}_{kj} \mathbf{F}_k \mathbf{E}_{kj}^{\mathrm{H}},\ \bar{\mathbf{D}}_{kj} = \mathbf{E}_{kj} \mathbf{F}_{\bar{k}} \mathbf{E}_{kj}^{\mathrm{H}},\ \mathbf{E}_{kj} = \left[\mathbf{h}_{kj}, h_0 \mathbf{P}_k^{\mathrm{H}} \hat{\mathbf{g}}_{kj}^{(i-1)}\right]^{\mathrm{H}},\ \mathbf{P}_k = \mathbf{\Theta}_k \hat{\mathbf{H}}^{(i-1)}, \tag{41a}$$

$$\mathcal{W}_1 = h_0 \sigma_s^2 \|(\hat{\mathbf{g}}_{kj}^{(i-1)})^{\mathrm{H}} \mathbf{\Theta}_k\|^2,\ \mathcal{W}_2 = \frac{\bar{\mathcal{W}} - \sigma_s^2 \sum_{k \in \mathcal{K}} \|\mathbf{\Theta}_k\|_F^2}{h_0 \sum_{k \in \mathcal{K}} \big(\sum_{k' \in \mathcal{K}} \mathrm{Tr}(\mathbf{P}_k \mathbf{F}_{k'} \mathbf{P}_k^{\mathrm{H}})\big)}, \tag{41b}$$

$$\mathcal{W}_3 = \frac{\zeta_m - \sigma_s^2 (1 - \alpha_m)}{h_0 (1 - \alpha_m) \sum_{k \in \mathcal{K}} \mathrm{Tr}\left(\bar{\mathbf{T}}_m \hat{\mathbf{H}}^{(i-1)} \mathbf{F}_k (\hat{\mathbf{H}}^{(i-1)})^{\mathrm{H}} \bar{\mathbf{T}}_m^{\mathrm{H}}\right)}. \tag{41c}$$

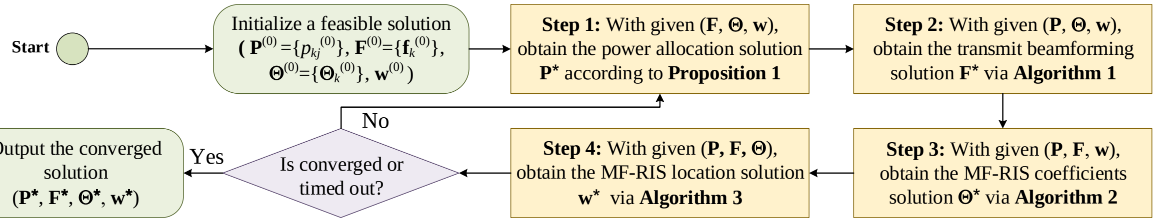

Fig. 3. A flowchart of the proposed AO algorithm.

TABLE III
SIMULATION PARAMETERS

Parameter	Value
Communication parameters	$h_0 = -20$ dB [20], $\kappa_0 = 2.2$, $\kappa_1 = 2.8$, $\kappa_2 = 2.6$, $\beta_0 = \beta_1 = \beta_2 = 3$ dB, $\sigma_u^2 = \sigma_s^2 = -70$ dBm
Power consumption parameters	$\xi = 1.1$, $P_b = 1.5$ mW, $P_{\text{DC}} = 0.3$ mW, $P_{\text{C}} = 2.1$ μW [21], $Z = 24$ mW, $a = 150$, $q = 0.014$ [34]
Other parameters	$N = 4$, $\beta_{\max} = 20$ dB [14], $\frac{d}{\lambda} = 0.5$, $\rho^{(0)} = 10^{-3}$, $\epsilon = 0.05$ [8]

Based on the above solutions, a flowchart of the overall AO algorithm for solving problem (14) is given in Fig. 3. Since the optimal power allocation is obtained in closed form in Proposition 1, the complexity of Step 1 is $\mathcal{O}(1)$. The complexity of the SDP problems in Steps 2 and 3 is $\mathcal{O}_{\mathbf{F}} = \mathcal{O}\big(I_{\mathbf{F}} \max(2N, 3J{+}M)^4\sqrt{2N}\big)$ and $\mathcal{O}_{\mathbf{\Theta}} = \mathcal{O}\big(I_{\mathbf{\Theta}} \max(2(M{+}1), 3J)^4 \sqrt{2(M+1)}\big)$, respectively, while the complexity of Step 4 using the interior-point method is $\mathcal{O}_{\mathbf{w}} = \mathcal{O}\big(I_{\mathbf{w}}(6{+}2M{+}11J)^{3.5}\big)$. Here, $I_{\mathbf{F}}$, $I_{\mathbf{\Theta}}$, and $I_{\mathbf{w}}$ represent the respective number of iterations [36]. Since each sub-algorithm converges to a local optimum, the objective value of problem (14) is non-decreasing after each iteration. Moreover, the maximum transmit power constraint (14c) indicates that the objective value has an upper bound. Hence, the AO algorithm is guaranteed to converge.

V. NUMERICAL RESULTS

In this section, numerical results are provided to validate the effectiveness of the proposed algorithm and the superiority of the considered MF-RIS assisted NOMA system. As shown in Fig. 4, we consider a scenario with $J_r = J_t = 2$ users, where the BS is located at $\mathbf{w}_b = [0, 0, 5]^{\text{T}}$ m and the MF-RIS deployable region is set as $\mathcal{P} = \{[5, y, 10]^{\text{T}} | 10 \le y \le 45\}$. Moreover, all users are randomly distributed in their own circle with the radius of 2 m. The corresponding centers are set as $[0, 30, 0]^{\text{T}}$, $[0, 35, 0]^{\text{T}}$, $[10, 40, 0]^{\text{T}}$, and $[10, 45, 0]^{\text{T}}$ m, respectively. Unless otherwise specified, we set $P_{\text{BS}}^{\max} = 40$ dBm and $M = 120$. Other parameters are summarized in Table III.

To evaluate the performance of the proposed algorithm, we consider four benchmarks, as summarized in Table IV, i.e.,

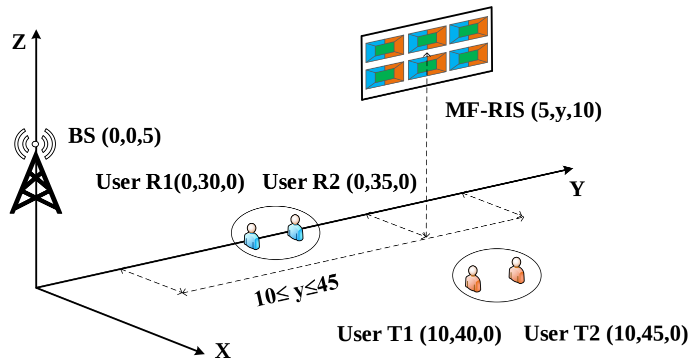

Fig. 4. Simulation setup.

TABLE IV
BENCHMARK ALGORITHMS

Algorithm	Power allocation	Transmit beamforming	MF-RIS coefficient	MF-RIS location
Exhaustive search-based algorithm	Exhaustive search	Algorithm 1	Algorithm 2	Exhaustive search
SDR-based algorithm	Proposition 1	SDR	SDR	Algorithm 3
MRT-based algorithm	Proposition 1	MRT	Algorithm 2	Algorithm 3
Random-based algorithm	Proposition 1	Algorithm 1	Random coefficient	Algorithm 3

- **Exhaustive search-based algorithm**: The power allocation factors and MF-RIS locations are optimized by the exhaustive search technique. This case can be regarded as providing a performance upper bound of our proposed algorithm.
- **SDR-based algorithm:** The transmit beamforming and MF-RIS coefficients are designed by adopting the SDR method, which ignores the rank-one constraints (29f) and (35d) [36]. The Gaussian randomization approach is applied when the obtained solution is not rank-one.
- **MRT-based algorithm:** The transmit beamforming optimization problem is solved by invoking the maximum-ratio transmission (MRT) method [7].
- **Random-based algorithm:** The MF-RIS coefficients are randomly set within the feasible region $\mathcal{R}_{\text{MF}} = \{\alpha_m, \beta_m^k, \theta_m^k | \alpha_m \in \{0,1\}, \beta_m^k \in [0, \beta_{\max}], \sum_{k\in\mathcal{K}} \beta_m^k \leq \beta_{\max}, \theta_m^k \in [0, 2\pi), \forall m, k\}$.

Fig. 5 shows the sum-rate versus $P_{\text{BS}}^{\max}$ under different algorithms. We observe that the proposed algorithm can achieve comparable performance to the exhaustive search-based algorithm with relatively low complexity. Specifically, the complexity of the proposed power allocation and MF-RIS location optimization algorithms is $\mathcal{O}(1)$ and $\mathcal{O}\big(I_{\mathbf{w}}(6 + 2M + 11J)^{3.5}\big)$, while the complexity of the exhaustive search with accuracy ς is $\mathcal{O}(\frac{1}{\varsigma^J})$ and $\mathcal{O}(\frac{1}{\varsigma^3})$, respectively. Due to the non-optimized MF-RIS coefficients, a significant performance loss is observed from the random-based algorithm compared to the proposed algorithm. Besides, the proposed algorithm achieves a higher performance gain than the SDR-based algorithm. This is because using the SDR method to solve the relaxed problem usually generates a high-rank solution, and the constructed

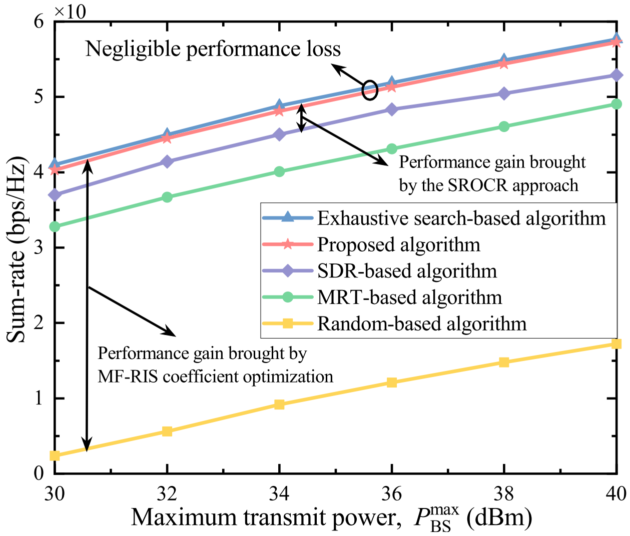

Fig. 5. Sum-rate versus $P_{\rm BS}^{\max}$ under different algorithms.

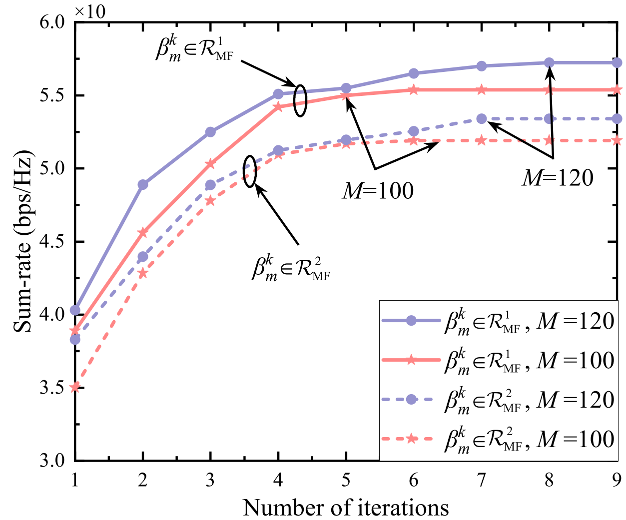

Fig. 6. Convergence behavior of the proposed AO algorithm under different M and different operating schemes.

solution is normally suboptimal or even infeasible for the original problem [37]. In contrast, the adopted SRCOR method can approach a locally optimal rank-one solution. Additionally, it is observed that the proposed algorithm outperforms the MRT-based algorithm, which confirms the importance of joint optimization of the transmit beamforming and other variables.

To demonstrate the benefits brought by the proposed MF-RIS, we consider the following schemes. Unless otherwise specified, the NOMA technique is adopted for all schemes.

- **MF-RIS with** $\beta_m^k \in \mathcal{R}_{\rm MF}^1 = \{\beta_m^k | \beta_m^k \in [0, \beta_{\max}], \sum_k \beta_m^k \leq \beta_{\max}, \forall m, k\}$: The BS is assisted by the proposed MF-RIS, where the elements operating in S mode reflect, refract, and amplify the incident signal simultaneously.
- **MF-RIS with** $\beta_m^k \in \mathcal{R}_{\rm MF}^2 = \{\beta_m^k | \beta_m^k \in [0, \beta_{\max}], \prod_k \beta_m^k = 0, \forall m, k\}$: This scheme considers a special case of the MF-RIS in which the elements operating in S mode are divided into two groups. One group is used to serve users in the front half-space (i.e., reflection), while the other group is used to serve users in the back half-space (i.e., refraction/transmission). This group-wise amplitude control reduces the overhead caused by exchanging configuration information between the BS and the MF-RIS, making it easier to implement in practical applications. Similar to the transformation for the product term $\alpha_m^2 \beta_m^k$ in constraint (37), the new intractable constraint, $\prod_k \beta_m^k = 0$, is tackled using CUB and penalty-based methods.
- **Active RIS [15]**: This type of RIS can amplify and reflect signals simultaneously, or refract and amplify signals simultaneously, but cannot support energy harvesting.

- **STAR-RIS [9]**: The communications from the BS to all users are assisted by a STAR-RIS, i.e., $\alpha_m = 1, \beta_m^k \in [0,1], \sum_k \beta_m^k \leq 1, \theta_m^k \in [0, 2\pi), \forall m, k$. Compared to the proposed MF-RIS, the STAR-RIS does not support signal amplification and energy harvesting.
- **Self-sustainable RIS [21]**: This type of RIS allows a portion of the elements to operate in signal reflection or refraction mode, while the remaining elements work in H mode.
- **Conventional RIS [7]**: In this scheme, the RIS only supports reflection or refraction.
- **Without RIS**: This is a baseline where no RIS is deployed. Only direct links are considered from the BS to the users.

To achieve full-space coverage, for the active RIS, self-sustainable RIS, and conventional RIS, one reflective RIS and one refractive RIS are deployed adjacent to each other at the same location as the MF-RIS, and each RIS has $M/2$ elements. In addition, for fairness, we define the total power budget as $P_{\rm total}^{\max}$, where $P_{\rm total}^{\max} = P_{\rm BS}^{\max} + P_{\rm RIS}^{\max}$ and $P_{\rm BS}^{\max} = P_{\rm RIS}^{\max}$ hold for the active RIS-aided schemes, and $P_{\rm total}^{\max} = P_{\rm BS}^{\max}$ holds for other schemes. Here, $P_{\rm RIS}^{\max}$ denotes the maximum amplification power at the active RIS.

The convergence behavior of the proposed algorithm with different numbers of MF-RIS elements and different operating schemes is illustrated in Fig. 6. It can be observed that all curves gradually increase and exhibit the trend of convergence after a finite number of iterations. Specifically, the proposed algorithm with $M = 100$ converges to a stable value after about 6 iterations. However, for the cases with $M = 120$, it requires around 8 iterations for convergence. This is because both the number of optimization variables and the number of constraints increase with M, and thus increase the complexity of solving problem (14).

Fig. 7 depicts the sum-rate versus the total power budget. For the two self-sustainable schemes, it is observed that the proposed MF-RIS is far superior to the self-sustainable RIS. To be specific, when $P_{\rm total}^{\max} = 40$ dBm, the MF-RIS assisted system enjoys 98.8% higher sum-rate gain than the system with self-sustainable RIS. This result can be explained as follows. On the one hand, compared to the MF-RIS, which adjusts its coefficients in an element-wise manner, the self-sustainable RIS only employs a fixed mode for each element. The latter suffers from performance loss due to its limited DoFs. On the other hand, the design of signal amplification can effectively alleviate the influence of “double attenuation” on the MF-RIS-aided links. This means that the proposed MF-RIS makes better use of the harvested energy and thus increases the sum-rate of all users. Additionally, compared to the conventional RIS, the MF-RIS achieves 23.4% higher performance gain by virtue of its resource allocation flexibility and signal amplification function.

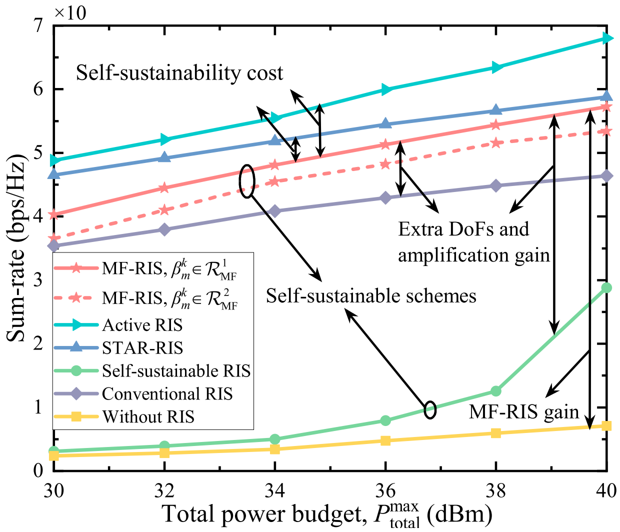

Fig. 7. Sum-rate versus $P_{\rm total}^{\rm max}$ under different schemes.

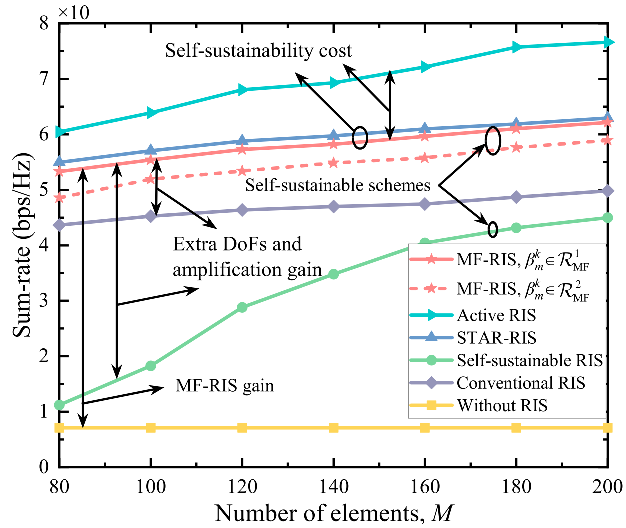

Fig. 8. Sum-rate versus M under different schemes.

We observe from Fig. 7 that the performance of active RIS and STAR-RIS is better than that of MF-RIS. This observation can be explained as follows: 1) the active RIS and the STAR-RIS use all elements to serve users, while the proposed MF-RIS only uses part of the elements to relay signals; 2) unlike the active RIS and the STAR-RIS, which assume an ideal lossless signal relay and power supply process, the MF-RIS takes into account the inevitable power loss and circuit consumption during energy harvesting and signal amplification. Although the self-sustainability of MF-RIS comes with the decreased performance, the sum-rate loss decreases with $P_{\rm total}^{\rm max}$ due to the fact that the elements operating in H mode can harvest more energy at high power. Besides, it is observed that the active RIS is superior to the STAR-RIS and the gain increases with $P_{\rm total}^{\rm max}$, indicating that a larger RIS amplification power allows the signal amplification gain to be greater than the gain of full-space coverage. Furthermore, we notice that for the MF-RIS, the scheme of $\beta_m^k \in \mathcal{R}_{\rm MF}^1$ always performs better than the scheme of $\beta_m^k \in \mathcal{R}_{\rm MF}^2$. This is because the magnitude coefficients of the former have a continuous feasible set $\mathcal{R}_{\rm MF}^1$, while those of the latter are restricted to a binary set $\mathcal{R}_{\rm MF}^2$. By employing a more flexible amplitude model, the MF-RIS with $\beta_m^k \in \mathcal{R}_{\rm MF}^1$ brings additional DoFs to each element to enhance the desired signal, eliminate inter-user interference, and thus increases the achievable sum-rate. Also, this phenomenon can be attributed to the fact that mathematically $\mathcal{R}_{\rm MF}^2$ is a special case of $\mathcal{R}_{\rm MF}^1$.

Fig. 8 illustrates the sum-rate versus the number of elements. It is shown that the sum-rate increases with M. This is because higher DoFs offered by larger size RISs can provide greater flexibility in beamforming, thus generating stronger cascaded channels. Notably, the active RIS

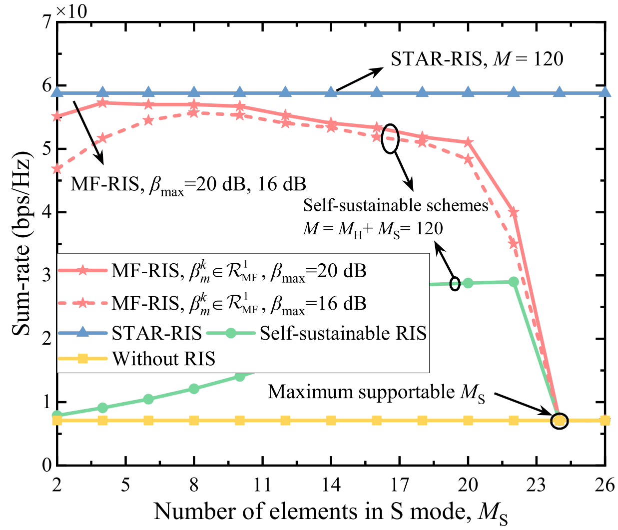

Fig. 9. Sum-rate versus $M_{\rm S}$ under different schemes.

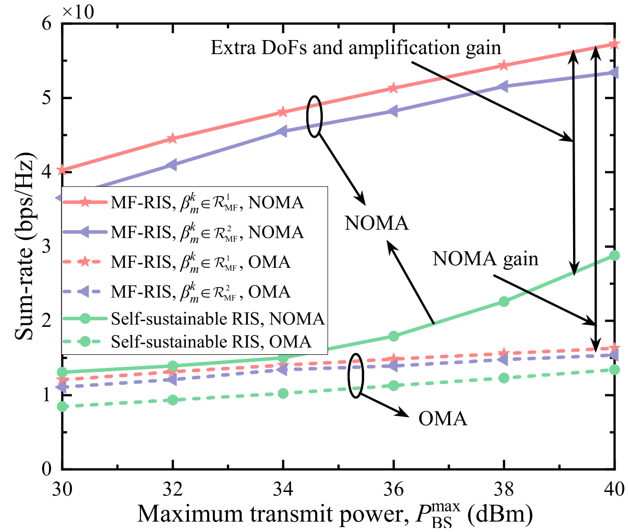

Fig. 10. Sum-rate versus $P_{\rm BS}^{\max}$ under different schemes.

outperforms the STAR-RIS in terms of sum-rate improvement as M increases, owing to its ability to directly amplify the signal. This highlights the importance of signal amplification function in improving the throughput performance of RIS-aided networks. Since a larger M means that there are more elements operating in S mode, the gap between the MF-RIS and the STAR-RIS becomes negligible. In contrast, maintaining self-sustainability for the self-sustainable RIS is costly. This further confirms that the proposed MF-RIS can effectively compensate for the performance loss caused by self-sustainability through full-space coverage and signal power enhancement.

In Fig. 9, we plot the sum-rate versus the number of elements operating in S mode to exhibit the relationship between sum-rate maximization and energy harvesting maximization. Here, we define $M_{\rm H}$ and $M_{\rm S}$ as the numbers of elements operating in H and S modes, respectively, satisfying $M_{\rm H} = M - \sum_{m\in\mathcal{M}} \alpha_m$ and $M_{\rm S} = \sum_{m\in\mathcal{M}} \alpha_m$. It is observed that the sum-rate of the MF-RIS first increases and then decreases as $M_{\rm S}$ increases, which deviates from the common sense for passive RISs that more signal relay elements always benefit. This is because the trade-off between $M_{\rm S}$ and $M_{\rm H}$ at a fixed M brings a trade-off between sum-rate and energy harvesting. Specifically, when $M_{\rm S}$ is small, the increase in $M_{\rm S}$ leads to a decrease in $M_{\rm H}$ and degrades the energy harvesting performance, but the relatively large $M_{\rm H}$ can harvest enough energy for the elements in S mode. Therefore, these signal relay elements can take advantage of reshaping the full-space wireless channels and mitigating their double attenuation to enhance signal reception.

Furthermore, Fig. 9 shows that the sum-rate decreases as $M_{\rm S}$ increases after reaching the optimal value. This is because that the decrease in $M_{\rm H}$ substantially restricts the energy that can be harvested, whereas the increase in M_{S} leads to higher circuit power consumption. Consequently, the available amplification power at the MF-RIS is significantly reduced, making the MF-RIS suffer more from the increased M_{S}. Moreover, when M_{S} exceeds the maximum supportable value, the limited harvested energy may not even maintain self-sustainability, resulting in the failure of self-sustainable RISs. Since a larger $\beta_{\max}$ generates a greater output power, the optimal M_{S} for the scheme of $\beta_{\max}=16$ dB is larger than that of $\beta_{\max}=20$ dB. These results indicate that a flexible element allocation strategy is crucial for self-sustainable RIS schemes to balance the trade-off between sum-rate and energy harvesting. In addition, a considerable performance gain is observed from the proposed MF-RIS and the self-sustainable RIS, verifying that the MF-RIS can better utilize the limited harvested power to enhance the sum-rate.

In Fig. 10, we compare the achievable performance of the considered NOMA and the conventional orthogonal multiple access (OMA) schemes. We observe that both the MF-RIS and the self-sustainable RIS under NOMA yield a larger sum-rate value than their corresponding OMA schemes. Particularly, when $P_{\mathrm{BS}}^{\max} = 40$ dBm, the NOMA systems assisted by the MF-RIS and the self-sustainable RIS provided up to 251% and 114.7% higher sum-rate gains than their OMA counterparts, respectively. The reason behind this is twofold. First, by serving all users within the same resource block, NOMA facilitates more flexible resource allocation to improve spectral efficiency. Second, the location and coefficient design of RIS enable a smart NOMA operation by intelligently tuning the direction of users' channel vectors. In addition, the MF-RIS gain over the self-sustainable RIS is again verified. The signal amplification capability allows MF-RIS to enhance the cascaded links, thereby combating the attenuation caused by the double path loss.

In Fig. 11, we investigate the achievable sum-rate versus the deployment strategy of RIS under different user location accuracy. In particular, we define τ as the location error of the user's actual location from the estimated location. Here, "Optimal location" invokes exhaustive search to obtain the optimal RIS location, while "Fixed location" fixes the 3D coordinate of RIS at $\mathbf{w} = [5, 20, 10]^{\mathrm{T}}$ m. Notably, the "Proposed algorithm" deployment strategy significantly outperforms the "Fixed location" algorithm, almost reaching the optimal performance. This is because the optimization of RIS location helps to unleash the full potential of RIS and NOMA, by providing a new DoF for their interplay. Another noteworthy phenomenon is that though the sum-rate achieved by the proposed algorithm decreases with the increase of user location errors, the gaps between our algorithm and the benchmark schemes remain stable. This shows that the proposed algorithm still has stable performance even at a low level of the location accuracy.

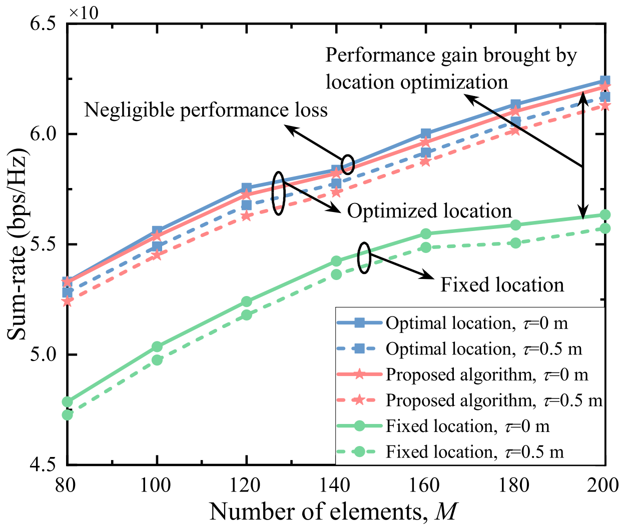

Fig. 11. Sum-rate versus M under different deployment strategies and different user location information.

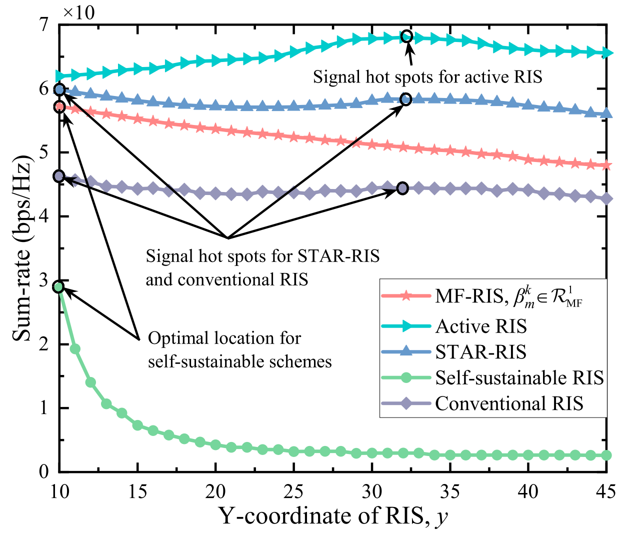

Fig. 12. Sum-rate versus y under different schemes.

In Fig. 12, we study the impact of RIS location on sum-rate by varying the Y-coordinate of RIS. It is interesting to remark that for the STAR-RIS scheme, the sum-rate first decreases and then increases as y increases, and decreases again after about $y = 30$ m. This trend can be explained as follows. First, since the channel gain is a decreasing function of the link distance, the STAR-RIS deployed in the vicinity of the BS or users creates signal hot spots. However, when the STAR-RIS is located at the middle between the BS and users, both the BS-RIS and RIS-user links experience severe signal attenuation, and the gain achieved by the cascaded links decreases accordingly. In contrast, the active RIS is less affected by double attenuation as it can provide more amplification gain to compensate for path loss when moving away from the BS. Besides, the reason for the inflection point is that deploying the STAR-RIS and active RIS near the user closer to the BS facilitates the exploitation of the channel gain differences among multiple NOMA users. When it comes to the self-sustainable RIS schemes, the sum-rate decreases as the RIS moves away from the BS. The optimal deployment location is the location closest to the BS within the allowable deployment range. Indeed, in order to maintain the balance between the energy supply and demand, both the MF-RIS and the self-sustainable RIS need to allocate more elements for energy harvesting when they are far away from the BS, resulting in fewer elements to relay signals. The above observations show that conventional RISs are able to obtain good performance when they are deployed near the transmitter or receiver, but for self-sustainable RISs, it would be better to deploy closer to the transmitter.

VI. Conclusions

In this paper, we proposed a new MF-RIS architecture enabling simultaneous signal reflection, refraction, amplification, and energy harvesting. The differences between the proposed MF-RIS and existing SF- and DF-RIS were first discussed from the perspective of the signal model. Next, we investigated the sum-rate maximization problem in an MF-RIS-aided NOMA network and the resulting MINLP problem was efficiently solved by an iterative algorithm. Furthermore, numerical results provided useful insights for practical system design, which, in particular, are 1) compared to the conventional passive RIS and self-sustainable passive RIS, the proposed MF-RIS can provide up to 23.4% and 98.8% performance gains, respectively, by integrating multiple functions on one surface; and 2) deploying MF-RIS closer to the transmitter side facilitates energy harvesting and therefore brings a higher performance gain. Although we have investigated the signal modeling and performance optimization problems of MF-RIS-aided wireless networks, there are still some important issues yet to be addressed, e.g.,

- *Practical implementation:* Compared to the prototype design of existing SF- and DF-RIS, the proposed MF-RIS faces new implementation challenges. For example, how to embed circuits that perform signal reflection, refraction, amplification, and energy harvesting functions into a limited substrate simultaneously, and how to balance the efficiency of these circuits.
- *High-accuracy channel estimation:* The proposed MF-RIS requires more pilot overhead than existing SF-RIS to estimate the reflection and refraction channels. Although simultaneously estimating all channels reduces the overhead, how to achieve fast and high-accuracy channel estimation requires further research.
- *Low-complexity deployment:* To make the proposed MF-RIS easy to deploy in practical systems, we can group the elements and set the same reflective/refractive amplitude for each group. Nevertheless, it remains open how to group the elements during practical deployment to attain desired performance with low complexity.

Appendix A
Proof of Lemma 1

Based on the rate expression in (9) and the equivalently combined channel gain γ_{kj}, we obtain

$$\bar{p}_{kj} = r_{kj}^{\min} \left(\sum\nolimits_{i=j+1}^{J_k} \bar{p}_{ki} + \frac{1}{\gamma_{kj}} \right). \tag{45}$$

According to [39, Proposition 1], the minimum transmit power is derived as

$$\sum\nolimits_{j\in\mathcal{J}_k} \bar{p}_{kj} = \sum\nolimits_{j\in\mathcal{J}_k} r_{kj}^{\min} \left(\sum\nolimits_{i=j+1}^{J_k} \bar{p}_{ki} + \frac{1}{\gamma_{kj}} \right) = \sum\nolimits_{j\in\mathcal{J}_k} \left(\prod\nolimits_{i=1}^{j-1} \left(r_{ki}^{\min} + 1 \right) \right) \frac{r_{kj}^{\min}}{\gamma_{kj}}. \tag{46}$$

Thus, in order to make problem (20) feasible, power allocation coefficients should satisfy (21).

APPENDIX B
PROOF OF PROPOSITION 1

Following the rate-splitting principle and defining the function $\Psi(x)=\log_2(1+x)$, we rewrite the achievable rate expression $R_{j\to j}^k$ as follows [40]:

$$R_{j\to j}^k \overset{(a)}{=} \Psi\Big[\frac{\gamma_{kj}p_{kj}}{\gamma_{kj}\sum_{i=j+1}^{J_k}p_{ki}+1}\Big] \overset{(b)}{=} \Psi\Big[\frac{\gamma_{kj}(\bar{p}_{kj}+\triangle p_{kj})}{\gamma_{kj}\sum_{i=j+1}^{J_k}p_{ki}+1}\Big] \tag{47a}$$

$$\overset{(c)}{=} \Psi\Big[\frac{\bar{p}_{kj}+r_{kj}^{\min}\sum_{i=j+1}^{J_k}\triangle p_{ki}}{\sum_{i=j+1}^{J_k}p_{ki}+\frac{1}{\gamma_{kj}}}\Big]+\Psi\Big[\frac{\triangle p_{kj}-r_{kj}^{\min}\sum_{i=j+1}^{J_k}\triangle p_{ki}}{\bar{p}_{kj}+r_{kj}^{\min}\sum_{i=j+1}^{J_k}\triangle p_{ki}+\sum_{i=j+1}^{J_k}p_{ki}+\frac{1}{\gamma_{kj}}}\Big] \tag{47b}$$

$$\overset{(d)}{=} \Psi\Big[\underbrace{\frac{\bar{p}_{kj}+r_{kj}^{\min}\sum_{i=j+1}^{J_k}\triangle p_{ki}}{\sum_{i=j+1}^{J_k}\bar{p}_{ki}+\sum_{i=j+1}^{J_k}\triangle p_{ki}+\frac{1}{\gamma_{kj}}}}_{r_{kj}^{\min}}\Big]+\Psi\Big[\underbrace{\frac{\triangle p_{kj}-r_{kj}^{\min}\sum_{i=j+1}^{J_k}\triangle p_{ki}}{\sum_{i=j}^{J_k}\bar{p}_{ki}+(1+r_{kj}^{\min})\sum_{i=j+1}^{J_k}\triangle p_{ki}+\frac{1}{\gamma_{kj}}}}_{\triangle r_{kj}^{\min}}\Big], \tag{47c}$$

where (b) follows from $p_{kj}=\bar{p}_{kj}+\triangle p_{kj}$, (c) holds due to the rate-splitting property [40], i.e., $\Psi(\frac{x+y}{z})=\Psi(\frac{x}{z})+\Psi(\frac{y}{x+z})$, and (d) is due to the fact that the following equation holds:

$$\bar{p}_{kj}+r_{kj}^{\min}\sum_{i=j+1}^{J_k}\triangle p_{ki}=r_{kj}^{\min}\left(\sum_{i=j+1}^{J_k}\bar{p}_{ki}+\frac{1}{\gamma_{kj}}\right)+r_{kj}^{\min}\sum_{i=j+1}^{J_k}\triangle p_{ki}. \tag{48}$$

To simplify the expression of $\triangle r_{kj}^{\min}$, we define

$$\triangle\hat{p}_{kj}=\big(\triangle p_{kj}-r_{kj}^{\min}\sum_{i=j+1}^{J_k}\triangle p_{ki}\big)\prod_{i=1}^{j-1}(1+r_{ki}^{\min}),\ \ \hat{p}_{kj}=\big(\sum_{i=j}^{J_k}\bar{p}_{ki}+\frac{1}{\gamma_{kj}}\big)\prod_{i=1}^{j-1}(1+r_{ki}^{\min}). \tag{49}$$

Based on (49), we then obtain the following equations:

$$\sum_{i=j+1}^{J_k}\triangle\hat{p}_{ki}=\prod_{i=1}^{j}(1+r_{ki}^{\min})\sum_{i=j+1}^{J_k}\triangle p_{ki},\quad \triangle r_{kj}^{\min}=\frac{\triangle\hat{p}_{kj}}{\hat{p}_{kj}+\sum_{i=j+1}^{J_k}\triangle\hat{p}_{ki}}. \tag{50}$$

As a result, problem (20) is reformulated as

$$\max_{\triangle\hat{p}_{kj}}\ \sum_{j\in\mathcal{J}_k}\Psi(r_{kj}^{\min})+\sum_{j\in\mathcal{J}_k}\Psi(\triangle r_{kj}^{\min}) \tag{51a}$$

$$\text{s. t.}\ \ \sum_{j\in\mathcal{J}_k}\triangle\hat{p}_{kj}=1-\sum_{j\in\mathcal{J}_k}\bar{p}_{kj}, \tag{51b}$$

where $\sum_{j\in\mathcal{J}_k}\Psi(r_{kj}^{\min})$ is a constant that does not affect the optimality of (51). Since the inequality $\hat{p}_{kj}\geq\hat{p}_{k(j+1)}$ holds and $\Psi(\triangle r_{kj}^{\min})$ increases with $\triangle r_{kj}^{\min}$, the optimal solution of (51) is to allocate all the excess power to user U_{kJ_k} with the best equivalent channel gain, i.e.,

$$\triangle\hat{p}_{kJ_k}=1-\sum_{j\in\mathcal{J}_k}\bar{p}_{kj},\quad \triangle\hat{p}_{kj}=0,\ \forall j\in\{\mathcal{J}_k/J_k\}. \tag{52}$$

Finally, the optimal power allocation coefficients and the corresponding objective value of problem (20) are obtained as (23) and (24), respectively.

APPENDIX C
PROOF OF CONSTRAINT (37)

We apply the penalty-based method to handle constraint $\eta_m^k=\alpha_m^2\beta_m^k$. Note that if we directly add it as a penalty term into the objective function (35a), (35a) will turn to $\sum_{k\in\mathcal{K}}\sum_{j\in\mathcal{J}_k}Q_{kj}$

$-\rho\sum_{k\in\mathcal{K}}\sum_{m\in\mathcal{M}}(\alpha_m^2\beta_m^k-\eta_m^k)$, where $\rho>0$ denotes the penalty factor. The resultant objective function is non-concave due to the term $\alpha_m^2\beta_m^k$. To this end, we replace it with its CUB [13]. Define the functions $g_1(\alpha_m,\beta_m^k)=\alpha_m^2\beta_m^k$ and $g_2(\alpha_m,\beta_m^k)=\frac{c_m^k}{2}\alpha_m^4+\frac{(\beta_m^k)^2}{2c_m^k}$, then it is easy to check that $g_2(\alpha_m,\beta_m^k)$ is a convex overestimate of $g_1(\alpha_m,\beta_m^k)$ for $c_m^k>0$. Moreover, when $c_m^k=\frac{\beta_m^k}{\alpha_m^2}$, the equations $g_1(\alpha_m,\beta_m^k)=g_2(\alpha_m,\beta_m^k)$ and $\nabla g_1(\alpha_m,\beta_m^k)=\nabla g_2(\alpha_m,\beta_m^k)$ hold, where $\nabla g_1(\alpha_m,\beta_m^k)$ and $\nabla g_2(\alpha_m,\beta_m^k)$ are the gradients of $g_1(\alpha_m,\beta_m^k)$ and $g_2(\alpha_m,\beta_m^k)$, respectively.

APPENDIX D
PROOF OF CONSTRAINT (43)

We define the slack variable set $\Delta_2=\{t,t_{kj},\bar{t}_{kj},e_{kj},v,\bar{v},r_{kj},\bar{r}_{kj},s_{kj}\}$ as

$$t=d_{bs}^{-\frac{\kappa_0}{2}},\ t_{kj}=d_{skj}^{-\frac{\kappa_2}{2}},\ \bar{t}_{kj}=tt_{kj},\ e_{kj}=d_{skj}^{-\kappa_2},\ v=\bar{v}=d_{bs}^{-\kappa_0}, \tag{53a}$$

$$r_{kj}=\bar{r}_{kj}=\bar{\mathbf{d}}_{kj}^{\mathrm{T}}\mathbf{D}_{kj}\bar{\mathbf{d}}_{kj},\ s_{kj}=\bar{\mathbf{d}}_{kj}^{\mathrm{T}}\bar{\mathbf{D}}_{kj}\bar{\mathbf{d}}_{kj}. \tag{53b}$$

Constraints (40a) and (40b) are then, respectively, rewritten as

$$t\le d_{bs}^{-\frac{\kappa_0}{2}},\ t_{kj}\le d_{skj}^{-\frac{\kappa_2}{2}},\ e_{kj}\ge d_{skj}^{-\kappa_2},\ v\ge d_{bs}^{-\kappa_0},\ \bar{v}\le d_{bs}^{-\kappa_0},\ r_{kj}\le\bar{\mathbf{d}}_{kj}^{\mathrm{T}}\mathbf{D}_{kj}\bar{\mathbf{d}}_{kj}, \tag{54a}$$

$$\bar{t}_{kj}\le tt_{kj},\ \bar{r}_{kj}\ge\bar{\mathbf{d}}_{kj}^{\mathrm{T}}\mathbf{D}_{kj}\bar{\mathbf{d}}_{kj},\ s_{kj}\ge\bar{\mathbf{d}}_{kj}^{\mathrm{T}}\bar{\mathbf{D}}_{kj}\bar{\mathbf{d}}_{kj}, \tag{54b}$$

$$A_{kj}^{-1}\le r_{kj},\ B_{kj}\ge s_{kj}+e_{kj}\mathcal{W}_1+\sigma_u^2,\ C_{kj}\ge\bar{r}_{kj}P_{kj}+B_{kj},\ v\le\mathcal{W}_2,\ \bar{v}\ge\mathcal{W}_3. \tag{54c}$$

Since constraints in (54a) are still non-convex, we apply the SCA method to deal with them. Specifically, by exploiting the first-order Taylor expansion of $\bar{\mathbf{d}}_{kj}^{\mathrm{T}}\mathbf{D}_{kj}\bar{\mathbf{d}}_{kj}$ at the given point $\{\bar{\mathbf{d}}_{kj}^{(\ell)}\}$, constraint $r_{kj}\le\bar{\mathbf{d}}_{kj}^{\mathrm{T}}\mathbf{D}_{kj}\bar{\mathbf{d}}_{kj}$ is recast as the following convex one:

$$r_{kj}\le-(\bar{\mathbf{d}}_{kj}^{(\ell)})^{\mathrm{T}}\mathbf{D}_{kj}\bar{\mathbf{d}}_{kj}^{(\ell)}+2\Re\big((\bar{\mathbf{d}}_{kj}^{(\ell)})^{\mathrm{T}}\mathbf{D}_{kj}\bar{\mathbf{d}}_{kj}\big). \tag{55}$$

To facilitate the derivation of the other constraints in (54a), we rewrite them as follows:

$$x^2+x_b^2+y^2+y_b^2+z^2+z_b^2-2x_bx-2y_by-2z_bz-t^{-\frac{4}{\kappa_0}}\le0, \tag{56a}$$

$$x^2+x_{kj}^2+y^2+y_{kj}^2+z^2-2x_{kj}x-2y_{kj}y-t_{kj}^{-\frac{4}{\kappa_2}}\le0, \tag{56b}$$

$$-x^2-x_{kj}^2-y^2-y_{kj}^2-z^2+2x_{kj}x+2y_{kj}y+e_{kj}^{-\frac{2}{\kappa_2}}\le0, \tag{56c}$$

$$-x^2-x_b^2-y^2-y_b^2-z^2-z_b^2+2x_bx+2y_by+2z_bz+v^{-\frac{2}{\kappa_0}}\le0, \tag{56d}$$

$$x^2+x_b^2+y^2+y_b^2+z^2+z_b^2-2x_bx-2y_by-2z_bz-\bar{v}^{-\frac{2}{\kappa_0}}\le0. \tag{56e}$$

The existence of non-convex terms $-t^{-\frac{4}{\kappa_0}}$, $-t_{kj}^{-\frac{4}{\kappa_2}}$, $-\bar{v}^{-\frac{2}{\kappa_0}}$, $-x^2$, $-y^2$, and $-z^2$ makes constraints (56) non-convex. Based on the SCA method, by replacing these non-convex terms with their respective convex first-order Taylor expansions, we obtain the convex constraints (43c)-(43g).

REFERENCES

[1] Q. Wu and R. Zhang, "Towards smart and reconfigurable environment: Intelligent reflecting surface aided wireless network," *IEEE Commun. Mag.*, vol. 58, no. 1, pp. 106-112, Jan. 2020.

[2] Y. Liu *et al.*, "Reconfigurable intelligent surfaces: Principles and opportunities," *IEEE Commun. Surveys Tuts.*, vol. 23, no. 3, pp. 1546-1577, 3rd Quart., 2021.

[3] K. Liu, Z. Zhang, L. Dai, and L. Hanzo, "Compact user-specific reconfigurable intelligent surfaces for uplink transmission," *IEEE Trans. Commun.*, vol. 70, no. 1, pp. 680-692, Jan. 2022.

[4] W. Ni, X. Liu, Y. Liu, H. Tian, and Y. Chen, "Resource allocation for multi-cell IRS-aided NOMA networks," *IEEE Trans. Wireless Commun.*, vol. 20, no. 7, pp. 4253-4268, Jul. 2021.

[5] W. Wang *et al.*, "Beamforming and jamming optimization for IRS-aided secure NOMA networks," *IEEE Trans. Wireless Commun.*, vol. 21, no. 3, pp. 1557-1569, Mar. 2022.

[6] W. Wang, H. Tian, and W. Ni, "Secrecy performance analysis of IRS-aided UAV relay system," *IEEE Wireless Commun. Lett.*, vol. 10, no. 12, pp. 2693-2697, Dec. 2021.

[7] Q. Wu and R. Zhang, "Beamforming optimization for wireless network aided by intelligent reflecting surface with discrete phase shifts," *IEEE Trans. Commun.*, vol. 68, no. 3, pp. 1838-1851, Mar. 2020.

[8] X. Mu, Y. Liu, L. Guo, J. Lin, and R. Schober, "Joint deployment and multiple access design for intelligent reflecting surface assisted networks," *IEEE Trans. Wireless Commun.*, vol. 20, no. 10, pp. 6648-6664, Oct. 2021.

[9] Y. Liu *et al.*, "STAR: Simultaneous transmission and reflection for 360° coverage by intelligent surfaces," *IEEE Wireless Commun.*, vol. 28, no. 6, pp. 102-109, Dec. 2021.

[10] X. Mu, Y. Liu, L. Guo, J. Lin, and R. Schober, "Simultaneously transmitting and reflecting (STAR) RIS aided wireless communications," *IEEE Trans. Wireless Commun.*, vol. 21, no. 5, pp. 3083-3098, May 2022.

[11] H. Zhang *et al.*, "Intelligent omni-surfaces for full-dimensional wireless communications: Principle, technology, and implementation," *IEEE Commun. Mag.*, vol. 60, no. 2, pp. 39-45, Feb. 2022.

[12] C. Wu, Y. Liu, X. Mu, X. Gu, and O. A. Dobre, "Coverage characterization of STAR-RIS networks: NOMA and OMA," *IEEE Commun. Lett.*, vol. 25, no. 9, pp. 3036-3040, Sept. 2021.

[13] W. Wang, W. Ni, H. Tian, Z. Yang, C. Huang, and K. -K. Wong, "Safeguarding NOMA networks via reconfigurable dual-functional surface under imperfect CSI," *IEEE J. Sel. Topics Signal Process.*, vol. 16, no. 5, pp. 950-966, Aug. 2022.

[14] R. Long, Y. -C. Liang, Y. Pei, and E. G. Larsson, "Active reconfigurable intelligent surface-aided wireless communications," *IEEE Trans. Wireless Commun.*, vol. 20, no. 8, pp. 4962-4975, Aug. 2021.

[15] Z. Zhang *et al.*, "Active RIS vs. passive RIS: Which will prevail in 6G?," *IEEE Trans. Commun.*, vol. 71, no. 3, pp. 1707-1725, Mar. 2023.

[16] K. Liu, Z. Zhang, L. Dai, S. Xu, and F. Yang, "Active reconfigurable intelligent surface: Fully-connected or sub-connected?," *IEEE Commun. Lett.*, vol. 26, no. 1, pp. 167-171, Jan. 2022.

[17] C. You and R. Zhang, "Wireless communication aided by intelligent reflecting surface: Active or passive?," *IEEE Wireless Commun. Lett.*, vol. 10, no. 12, pp. 2659-2663, Dec. 2021.

[18] N. Shlezinger, G. C. Alexandropoulos, M. F. Imani, Y. C. Eldar, and D. R. Smith, "Dynamic metasurface antennas for 6G extreme massive MIMO communications," *IEEE Wireless Commun.*, vol. 28, no. 2, pp. 106-113, Apr. 2021.

[19] Y. Zou, S. Gong, J. Xu, W. Cheng, D. T. Hoang, and D. Niyato, "Wireless powered intelligent reflecting surfaces for enhancing wireless communications," *IEEE Trans. Veh. Technol.*, vol. 69, no. 10, pp. 12369-12373, Jul. 2020.

[20] B. Lyu, P. Ramezani, D. T. Hoang, S. Gong, Z. Yang, and A. Jamalipour, "Optimized energy and information relaying in self-sustainable IRS-empowered WPCN," *IEEE Trans. Commun.*, vol. 69, pp. 619-633, Oct. 2021.

[21] S. Hu, Z. Wei, Y. Cai, C. Liu, D. W. K. Ng, and J. Yuan, "Robust and secure sum-rate maximization for multiuser MISO downlink systems with self-sustainable IRS," *IEEE Trans. Commun.*, vol. 69, no. 10, pp. 7032-7049, Oct. 2021.

[22] S. Kim *et al.*, "Ambient RF energy-harvesting technologies for self-sustainable standalone wireless sensor platforms," *Proc. IEEE*, vol. 102, no. 11, pp. 1649-1666, Nov. 2014.

[23] A. S. Almansouri, M. H. Ouda, and K. N. Salama, "A CMOS RF-to-DC power converter with 86% efficiency and -19.2-dbm sensitivity," *IEEE Trans. Microw. Theory Techn.*, vol. 66, no. 5, pp. 2409-2415, May 2018.

[24] L. Dai *et al.*, "Reconfigurable intelligent surface-based wireless communications: Antenna design, prototyping, and experimental results," *IEEE Access*, vol. 8, pp. 45913-45923, 2020.

[25] NTT DOCOMO, "DOCOMO conducts world's first successful trial of transparent dynamic metasurface," Jan. 2020. [Online]. Available: https://www.nttdocomo.co.jp/english/info/media_center/pr/2020/0117_00.html.

[26] S. Zeng *et al.*, "Intelligent omni-surfaces: Reflection-refraction circuit model, full-dimensional beamforming, and system implementation," *IEEE Trans. Commun.*, vol. 70, no. 11, pp. 7711-7727, Nov. 2022.

[27] K. W. Choi *et al.*, "Toward realization of long-range wireless-powered sensor networks," *IEEE Wireless Commun.*, vol. 26, no. 4, pp. 184-192, Aug. 2019.

[28] F. Amato, C. W. Peterson, B. P. Degnan, and G. D. Durgin, "Tunneling RFID tags for long-range and low-power microwave applications," *IEEE J. Radio Freq. Identificat.*, vol. 2, no. 2, pp. 93-103, Jun. 2018.

[29] D. C. Erb, O. C. Onar, and A. Khaligh, "An integrated bi-directional power electronic converter with multi-level AC-DC/DC-AC converter and non-inverted buck-boost converter for PHEVs with minimal grid level disruptions," in *Proc. IEEE Vehicle Power Propuls. Conf.*, Lille, France, Sept. 2010, pp. 1-6.

[30] S. P S, V. Suresh Babu, and G. Shiny, "Annealing effects on capacitance density and voltage coefficient of capacitance (VCC) of thin-film capacitor for energy harvesting application," in *Proc. TEQIP III Spons. Int. Conf. Microw. Integr. Circuits Photon. Wireless Netw.*, Tiruchirappalli, India, May 2019, pp. 223-227.

[31] Z. Zeng, S. Shen, B. Wang, J. J. Estrada-Lopez, R. Murch, and E. Sanchez-Sinencio, "An ultra-low-power power management circuit with output bootstrapping and reverse leakage reduction function for RF energy harvesting," in *Proc. IEEE MTT-S Int. Microw. Symp. Dig.*, Los Angeles, CA, USA, Aug. 2020, pp. 1059-1062.

[32] D. Tse and P. Viswanath, *Fundamentals of Wireless Communication.* Cambridge, U.K.: Cambridge Univ. Press, 2005.

[33] J. Zuo, Y. Liu, Z. Ding, L. Song, and H. V. Poor, "Joint design for simultaneously transmitting and reflecting (STAR) RIS assisted NOMA systems," *IEEE Trans. Wireless Commun.*, vol. 22, no. 1, pp. 611-626, Jan. 2023.

[34] P. Zeng, Q. Wu, and D. Qiao, "Energy minimization for IRS-aided WPCNs with non-linear energy harvesting model," *IEEE Commun. Lett.*, vol. 10, no. 11, pp. 2592-2596, Nov. 2021.

[35] J. Cui, Z. Ding, P. Fan, and N. Al-Dhahir, "Unsupervised machine learning-based user clustering in millimeter-wave-NOMA systems," *IEEE Trans. Wireless Commun.*, vol. 17, no. 11, pp. 7425-7440, Nov. 2018.

[36] Z.-Q. Luo, W.-K. Ma, A. So, Y. Ye, and S. Zhang, "Semidefinite relaxation of quadratic optimization problems," *IEEE Signal Process. Mag.*, vol. 27, no. 3, pp. 20-34, May 2010.

[37] P. Cao, J. Thompson, and H. V. Poor, "A sequential constraint relaxation algorithm for rank-one constrained problems," in *Proc. Eur. Signal Process. Conf.*, Kos, Greece, Aug. 2017, pp. 1060-1064.

[38] M. Grant and S. Boyd, "CVX: Matlab software for disciplined convex programming, version 2.1," [Online]. Available: http: //cvxr.com/cvx/, 2014.

[39] J. Cui, Z. Ding, and P. Fan, "A novel power allocation scheme under outage constraints in NOMA systems," *IEEE Signal Process. Lett.*, vol. 23, no. 9, pp. 1226-1230, Sept. 2016.

[40] N. Jindal and A. Goldsmith, "Capacity and optimal power allocation for fading broadcast channels with minimum rates," *IEEE Trans. Inf. Theory*, vol. 49, no. 11, pp. 2895-2909, Nov. 2003.